Basics of Synthetic Aperture Radar Interferometry and Applications

Roland Klees and Ramon Hanssen
Physical Geometrical and Space Geodesy Section
Department of Geodesy, Faculty of Civil Engineering and Geosciences
Delft University of Technology, The Netherlands
e-mail: klees@geo.tudelft.nl

Nordic Geodetic Commission (NKG) Autumn School: 28 August – 2 September, 2000 in Fevik, Norway 'Nordic Geodesy towards the 21st Century'

Contents

1 Introduction

The purpose of these lecture notes is to introduce the basic principles of SAR Interferometry (InSAR), and to discuss some of the applications of InSAR for the monitoring of deformations. Therefore, the treatment has been simplified to provide a starting point for the interested reader who wants to know how InSAR works and to get a basic grasp of InSAR theory and terminology. The paper does not intend to serve as a reference for experienced researchers. In order to avoid an exhaustive list of references it is limited to some review papers, which may be the starting point for a more detailed literature study.

It is about 40 years ago that it was observed that a side-looking imaging radar operating on wavelengths in the order of centimeters can be used to map the Earth's surface with a resolution of some meters without requiring huge antennas. Already NASA's Seasat-A, launched in 1978, and, since 1991, ESA's ERS-1, showed a wide variety of applications of this technique, which is called Synthetic Aperture Radar (SAR). Examples are the study of geological structures and the classification of rock type, the study of ocean waves and currents, the characteristics of ice, the detection of ship wakes, and the mapping of land use. The use of SAR as an interferometer is rather new due to the stringent requirements on the stability of the satellite orbit. InSAR offers the possibility to map the Earth's land and ice topography and to measure small displacements over large temporal and spatial scales with subcentimeter accuracy, independently of the sun's illumination and the cloud coverage. These properties make InSAR a unique technique which combines the high accuracy of classical geodetic techniques such as GPS and leveling with the imaging property of classical remote sensing techniques. Recent examples have demonstrated that InSAR can be applied to study a variety of deformation processes, e.g. land subsidence due to mining activities and due to the withdrawal of water, gas, and oil, the co-seismic and post-seismic displacement field related to earthquakes, the deflation and inflation of volcanos, the dynamics of glaciers and ice sheets, tectonic processes, orogenesis and erosion, and coastal zone changes.

The interferometric processing of SAR signals allows not only to infer surface changes from the radar images. It was already mentioned that InSAR can be used to derive high resolution digital elevation maps, as well. Other potential new applications are e.g. the study of the electrical properties of the Earth's surface, including water content, the land classification, and the mapping of flooded areas. These aspects will be out of the scope of these lecture notes.

2 Basic Principles

In this section a brief review of the basic principles of InSAR for topographic mapping and deformation monitoring is given. First, the geometry of an imaging radar will be outlined, followed by a discussion of the interferometric approach. For questions on radar

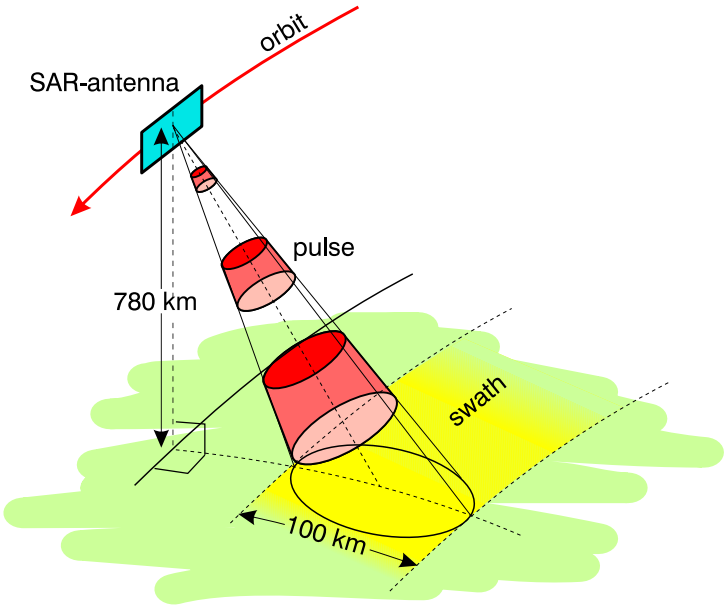

Figure 1: Geometry of a spaceborne imaging radar.

system operation and signal processing the interested reader may consult a general text on radar remote sensing, e.g. (Curlander and McDonough, 1991).

2.1 Imaging SAR geometry

A SAR is an imaging radar device that records the radar backscatter of the Earth's surface. An antenna, mounted on a spacecraft transmits periodically pulses in a side-looking direction w.r.t. the spacecraft's direction of motion. A part of the radar pulse energy is backscattered from the surface of the Earth and received a fraction of a second later at the same antenna. The brightness (*amplitude*), the round-trip time (*slant range*), and the *phase* relative to a stable reference oscillator are measured and recorded to construct the image (Figure 1).

The typical size of the illuminated area is about 100 km for today's spacecraft systems. The nominal resolution in the direction of illumination, the so-called *range direction*, is about 9 m, and in the direction of the spacecraft's motion, the *azimuth direction*, it is about 5 m. The resolution on the ground depends on the look angle θ. Assuming $\theta = 23°$, which corresponds to the mean look angle of the ERS-satellites, we obtain a resolution cell of about 25×5 m^2. Usual applications of SAR make only use of the amplitude information in just *one* image. InSAR, however, makes use mainly of the *phase* measurements in *two or more* SAR images of the same scene, acquired at two different instants and/or at two slightly different locations. This is made possible since SAR is a coherent imaging system retaining phase information in the radar echo during data acquisition and subsequent processing. By interference of the two images, we can infer very small slant range changes in two SAR images of the same surface. These slant range changes can be

related to topography and/or surface deformations. Since SAR is an imaging system, this information is available for each pixel. One full scene (100×100 km^2) contains roughly 10^8 pixels, meaning that SAR provides an almost continuous picture of the topography and/or the deformation field within the scene.

To get an idea how it works the relation between the total phase Φ and the distance between antenna and pixel, the *slant range* r is considered first. It is given by the simple formula (cf. Figure 2).

$$\Phi = -2\pi \cdot \frac{2r}{\lambda} + \Phi_{scat}\,. \tag{1}$$

That means, the total phase Φ at each point is equal to the sum of a *propagation part*, proportional to the round-trip distance $2r$, and a *scattering part* Φ_{scat} due to the interaction of the wave with the ground. The radar wavelength is denoted by λ, which is, e.g., 5.66 cm for the ERS SAR. The scattering part Φ_{scat} cannot be determined and remains unknown. Therefore, when making use of just one image, it is never possible to infer the slant range from the measured phase due to the unknown phase shift Φ_{scat}. Now, it is

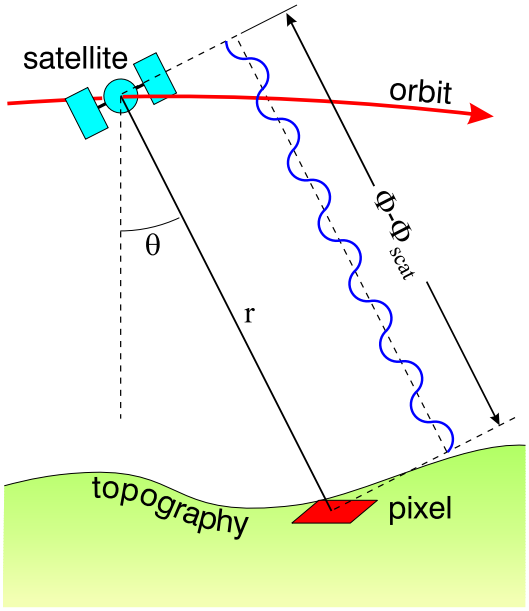

Figure 2: Slant range - phase relation, equation (1)

assumed that we take two images of the same scene at two distinguished time instants t_1 and t_2 from exactly the same location in space (Figure 3). If the elementary scatterers within each pixel are undisturbed in the time between the two image acquisitions, the scattering part Φ_{scat} does not change. Thus, the phase difference (for simplicity reasons the notation Φ is used again) is independent of the scattering mechanism, and becomes a measure of the line-of-sight component $\Delta r = r_1 - r_2$ of the target displacement vector

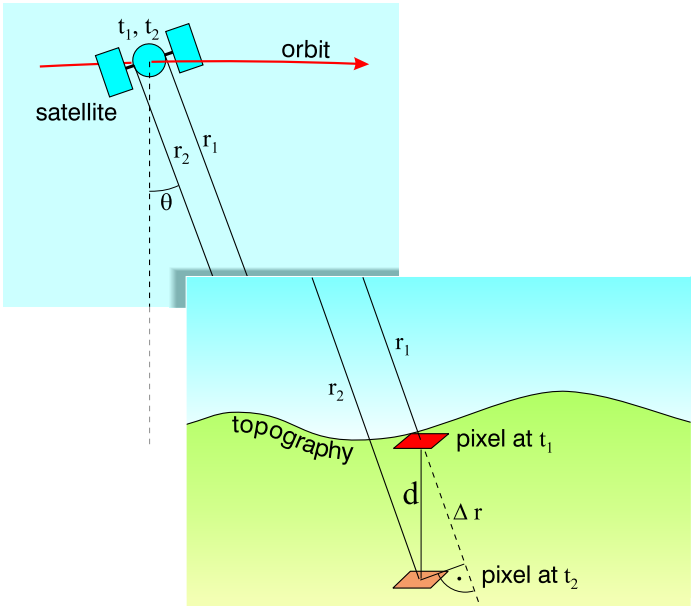

Figure 3: Geometry of zero-baseline SAR Interferometry.

over the time interval $[t_1, t_2]$:

$$\Phi = 2\pi \cdot \frac{2\Delta r}{\lambda} \,. \tag{2}$$

So, given the phase difference Φ, the component of the displacement in *range direction* can be determined pixel-by-pixel. The phase can be measured with an accuracy of a fraction of the radar wavelength, i.e. accurate to a few millimeters for today's satellite SAR systems.

A second image of the same scene can be obtained in various ways (cf. Figure 4). One possibility is to mount two physical antennas on a single platform. Only one antenna transmits the signals but both antennas receive it. This is the usual approach for aircraft implementations (cf. top left panel of Figure 4). The advantage is that temporal changes of Φ_{scat} have no influence because the images are taken simultaneously. However, because the size of the fuselage limits the baseline length, the phase difference is less sensitive to heights (cf. Section 3), which must be balanced by using shorter wavelengths (< 1 cm). This implementation has also been used in the U.S./German/Italian SRTM mission, flown in February 2000, where the second antenna was mounted at a boom of about 60 m length, which then formed the interferometer baseline (cf. bottom right panel of Figure 4). A second possibility is to utilize a single antenna on a satellite in a nearly exact-repeating orbit (cf. top right panel of Figure 4). After a fixed number of days, the so-called *repeat period*, the satellite ground track repeats with an accuracy of better than 1 km. Therefore, the same scene is imaged on two passes separated by the repeat period or an integer number of repeat periods. The advantage is that by carefully selecting the image pair, 'optimal' baselines can be obtained (cf. Section 3). The major drawback is

the repeat period, which varies between several days and some weeks, depending on the orbit parameters. Therefore, it becomes more likely that Φ_{scat} changes during the acquisition of the first and second image, and, by taking the phase difference, this term will not drop out, leading to noisy (less 'coherent') phase observations. This approach is the usual approach for spaceborne InSAR. For future missions alternative implementations are discussed as well. The one shown in the lower left panel of Figure 4 aims at combining the advantages of the two implementations mentioned before: two spacecrafts flying in formation are utilized, which makes longer baselines possible, and at the same time provides coherent phase observations. Common to all these InSAR implementations is the fact that we do not have a zero-baseline configuration as assumed in Figure 3. Hence the surface is not viewed twice from exactly the same location in space but from a slightly different location. This results in some range variation in the interferogram, which is the key for topographic mapping, but makes the extraction of deformations more elaborous, as will be shown in Section 2.2.

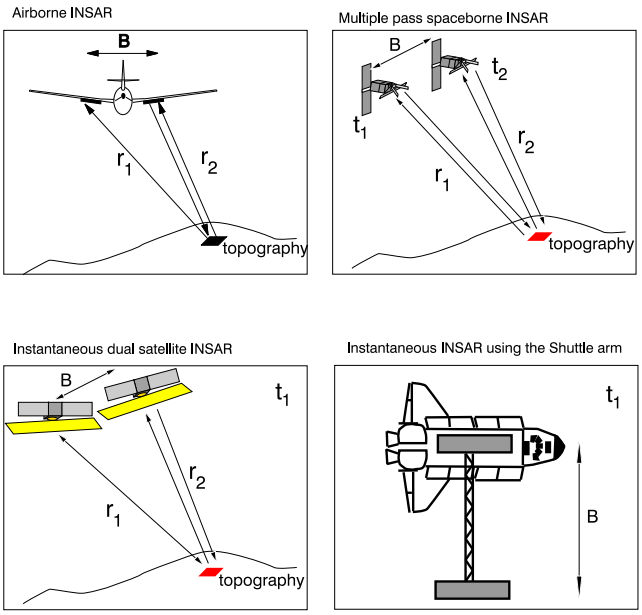

Figure 4: Various implementations of SAR Interferometry.

2.2 InSAR Geometry

In the following the term *SAR Interferometry* (InSAR) is used for all methods that employ the phase of the SAR signals in at least two complex-valued SAR images in order to derive information about the geometry and deformation of the Earth's surface. The usual configuration of this so-called *across-track* spaceborne InSAR is shown in Figure 5: two SAR's fly on ideally parallel tracks and view the terrain from slightly different directions. The separation of the flight paths is called *baseline*, its component perpendicular to some look direction the *perpendicular* or *effective baseline*, and its component parallel to some look direction the *parallel baseline*. This implies that in reality the second image

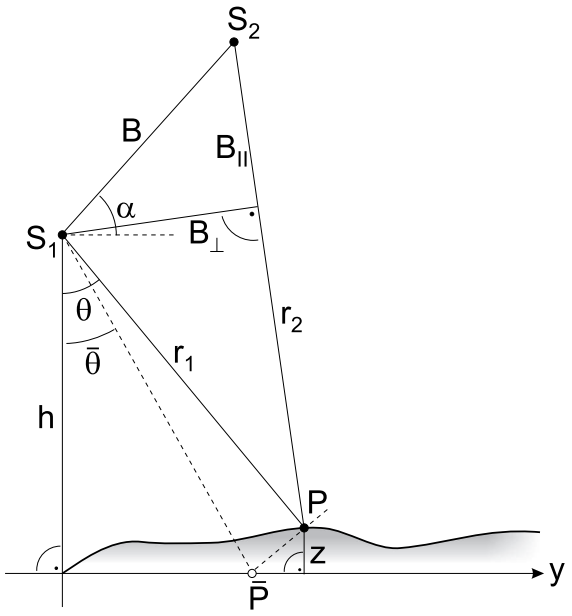

Figure 5: Geometry of across-track InSAR. The flight paths are perpendicular to the plane. The SAR illuminates the same pixel on ground from positions S_1 and S_2. The measured interferometric phase is proportional to the range difference $\delta r = r_1 - r_2$, which in turn is approximately equal to the parallel baseline $B_{\|}$, according to equation (5). It can be determined to a small fraction of a wavelength. Note that the SAR image acquired at S_1 does not allow to separate point P from $\bar{P}$ since both have the same distance r_1 to the SAR sensor S_1.

is not taken at exactly the same location as the first one (which is different from the zero-baseline configuration of Figure 3), and the phase difference Φ contains not only the radar line-of-sight component of the displacement vector but also some range differences due to the side-looking geometry and the topography.

In order to get some idea about these range differences, it is assumed that the geometry of the reference surface is flat (cf. Figure 5). For spaceborne sensors this flat geometry will usually not be accurate enough, but similar expressions as given next using a curved geometry may be derived easily. Forming the interferogram means computing the complex product of two complex-valued SAR images u_1 and u_2:

$$u_{int}(\cdot) = u_1 \cdot u_2^* = |u_1(\cdot)|e^{i\Phi_1} \cdot |u_2(\cdot)|e^{-i\Phi_2} = |u_1(\cdot)||u_2(\cdot)|e^{i(\Phi_1 - \Phi_2)}. \tag{3}$$

The total interferometric phase $\Phi := \Phi_1 - \Phi_2$ then becomes

$$\Phi = \arctan\left[\frac{Im(u_1(\cdot)u_2^*(\cdot))}{Re(u_1(\cdot)u_2^*(\cdot))}\right] = \varphi + 2\pi \cdot w, \qquad w \in \mathbb{Z}, \tag{4}$$

where $\varphi := W\{\Phi\} = \mathrm{mod}(\Phi, 2\pi) - \pi \in [-\pi, \pi)$, is called the *wrapped (fractional) interferometric phase*. W denotes the so-called wrapping operator. Of course, φ is still ambigous

to within integer multiples of 2π, and the phase ambiguity $2\pi \cdot w,\ w \in \mathbb{Z}$ first has to be determined pixel by pixel in order to determine the *absolute* or *unwrapped* interferometric phase Φ. This process is called *phase unwrapping*. Φ is directly proportional to the distance difference $\delta r := r_1 - r_2$:

$$\Phi_1 = -\frac{4\pi}{\lambda} r_1 + \Phi_{scat,1}, \quad \Phi_2 = -\frac{4\pi}{\lambda} r_2 + \Phi_{scat,2}$$
$$\Rightarrow\ \Phi = -\frac{4\pi}{\lambda}\delta r + (\Phi_{scat,1} - \Phi_{scat,2})\,.$$

That means, InSAR uses the phase information of two SAR images to measure the distance difference δr unlike stereo photogrammetry, where homologous points need to be identified, and parallaxes have to be measured directly. Once δr has been measured, the location of a point in a plane perpendicular to the (parallel) flight paths is found as the intersection of the circle r = constant and a hyperbola defined by δr = constant. δr is related to the look angle θ:

$$\begin{aligned} {r_2}^2 &= r_1^2 + B^2 - 2r_1 B\cos\left(\frac{\pi}{2} - (\theta - \alpha)\right) \\ \delta r &\approx B\sin(\theta-\alpha) - \frac{B^2}{2r_1}\cos^2(\theta-\alpha) + O\left(\frac{B^3}{r_1^2}\right) \\ \delta r &\approx B\sin(\theta-\alpha), \qquad B \ll r_1. \end{aligned} \tag{5}$$

Equation (5) shows that the distance difference δr is approximately equal to the parallel baseline. Moreover, it varies even for flat terrain due to the side-looking SAR. For constant slant-range r the look angle θ depends also on the terrain height z of the pixel above the reference surface:

$$\cos\theta(z) = \frac{h-z}{r} = \cos\bar{\theta} - \frac{z}{r},$$

where $\bar{\theta} = \theta(z=0)$, and h is the height of the radar sensor above the (flat) reference surface. When inserting this equation into equation (5), and making a Taylor series expansion, δr is obtained as function of the terrain height z

$$\delta r(z) = B\cdot\sin(\bar{\theta}-\alpha) + \frac{B\cdot\cos(\bar{\theta}-\alpha)}{r\cdot\sin\bar{\theta}}\cdot z - \frac{B\cos\alpha}{2r^2\sin^3\bar{\theta}}\cdot z^2 + O\left(\left(\frac{z}{r}\right)^3\right).$$

Using $\Phi = -\frac{4\pi}{\lambda}\delta r$, the equation, which describes the variation of the interferometric phase due to topography and deformations up to terms of order $O((z/r)^2)$, is obtained:

$$\Phi(z) = -\frac{4\pi}{\lambda}\big(B_{\|} + \frac{B_{\perp}}{r\cdot\sin\bar{\theta}}\cdot z + \Delta r), \tag{6}$$

where Δr denotes the line-of-sight component of the deformation vector, $B_{\|} = B\sin(\bar{\theta}-\alpha)$ the parallel baseline and $B_{\perp} = B\cos(\bar{\theta}-\alpha)$ the perpendicular baseline. Equation (6) shows that the total interferometric phase is the sum of three components: first, a component proportional to the parallel baseline for the reference surface, due to the viewing geometry, second, a component that expresses the range difference due to topographic

height variations relative to the reference surface, and third, a component that is proportional tothe line-of-sight surface displacement. Note that the effect of topography on the interferometric phase is scaled by the perpendicular baseline $B_\perp$, whereas the effect of the side-looking geometry and of the reference surface is determined by the parallel baseline $B_\parallel$.

The wrapped interferometric phase image is called *interferogram*. It shows pixel-by-pixel the wrapped interferometric phase of the complete scene. An example is given in Figure 6. It shows the area around Baja California in Mexico, near the boarder to California. The top panel is the amplitude image. In order to interprete the amplitude image correctly it may be assumed as a rule of thumb that calm water and smooth surfaces show up in black, while surface variations near the radar wavelength are bright, as are wind-roughened water surfaces if the resulting waves are of the order of the radar wavelength. Hills are mapped bright on one side and dim on the other; mountains look like 'lying down', and steep topography and small look angles makes this worse. The middle panel shows the wrapped interferometric phase, coded on a color wheel. One run through the color wheel corresponds to a complete rotation of 2π or $360°$ in interferometric phase. The dominant frequency is associated to the side-looking imaging geometry, i.e. due to the term $\Phi_{ref} = -\frac{4\pi}{\lambda} B_\parallel$; topography and line-of-sight deformations show up as local modulations of the dominating phase term Φ_{ref}. When subtracting the term Φ_{ref} a much smoother interferogram is obtained, which in the absence of line-of-sight deformations ($\Delta r = 0$), resembles an iso-height image (Figure 6, bottom panel).

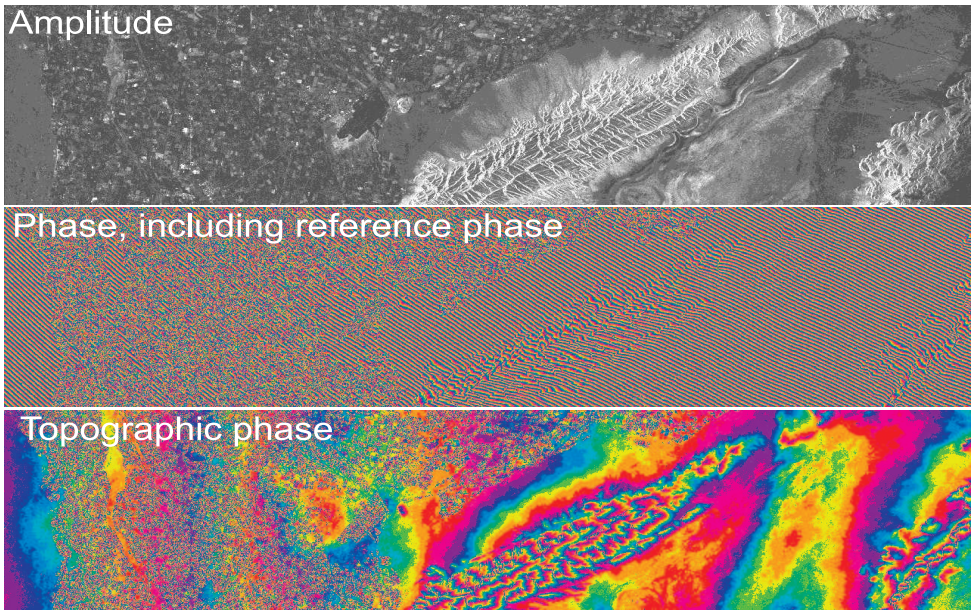

Figure 6: From top to buttom: amplitude image, total interferogram and topographic interferogram of the area around Baja California, Mexico. Note that the high frequency fringes in the middle panel are caused by the side-looking geometry, whereas the bottom panel only shows the low frequency fringe pattern of the topography in that area.

The height sensitivity of the interferometric phase is given by

$$|\frac{\partial \Phi(z)}{\partial z}| = \frac{4\pi}{\lambda}\frac{B_\perp}{r \sin \bar{\theta}}. \tag{7}$$

The height difference resulting in a phase change of one fringe (2π) is called the *height ambiguity*, $z_{2\pi}$:

$$z_{2\pi} = |\frac{\lambda}{2}\frac{r \sin \bar{\theta}}{B_\perp}|. \tag{8}$$

The smaller the height ambiguity the more sensitive the interferometer w.r.t. *topography*. Since λ is a system parameter and r and θ vary only slightly over a full scene, the sensitivity is obviously scaled by the perpendicular baseline $B_\perp$. The sensitivity increases with increasing perpendicular baseline, thus decreasing height ambiguity. Figure 7 shows the relation between the height of ambiguity and the perpendicular baseline. For the ERS satellites, the height ambiguity can be as low as 10 meters. Note that the sensitivity w.r.t. *deformations* is independent of the baseline and only depends on the radar wavelength λ.

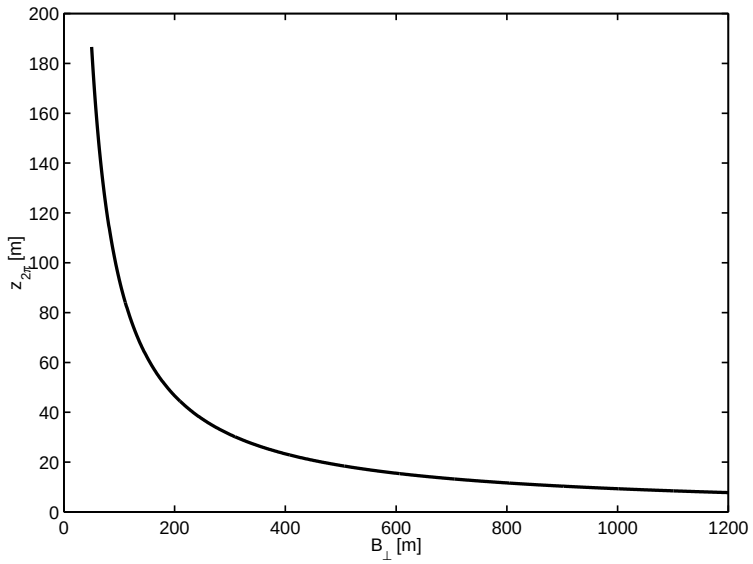

Figure 7: Relation between the perpendicular baseline $B_\perp$ and the height of ambiguity $z_{2\pi}$, equation (8). The larger the perpendicular baseline the more sensitive the interferometric phase w.r.t. height variations. Note that the maximum perpendicular baseline is limited, see Section 4.1 for more details.

3 The functional model

In this section the observation equations for InSAR are formulated. For more details the interested reader may consult (Hanssen, 2001).

Equation (6) describes approximately the relation between the total interferometric phase and both the topography and the deformation. In terms of the theory of parameter estimation in linear models it may be considered as an observation equation connecting the observed (fractional) interferometric phase with the primary unknowns 'topography' and 'line-of-sight deformation'. In reality this model has to be extended by at least two terms describing the slant atmospheric delay at the time epoch of the first and second image acquisition, respectively. Moreover, one has to take into account that the total interferometric phase can only be measured modulo 2π. When assuming that the reference surface term is first wrapped and then subtracted from the wrapped interferometric phase φ,

$$\psi_k := \varphi_k - W\{\kappa B_{||,k}\}, \tag{9}$$

where ψ is called the *flattened interferometric phase*, the observation equation for pixel k may be written as

$$\psi_k = -\kappa \frac{B_{\perp,k}}{r_k \cdot \sin\bar{\theta}_k} \cdot z_k + \kappa\, \Delta r_k + \kappa S_{k,t_1} - \kappa S_{k,t_2} - 2\pi \cdot w_k, \tag{10}$$

where $\kappa = \frac{4\pi}{\lambda}$. Equation (10) relates the flattened interferometric phase related to pixel k to 5 unknowns: the topographic height z_k, the deformation in slant-range direction Δr_k, the slant atmospheric delay during acquisitions t_1 and t_2, S_{k,t_1} and S_{k,t_2}, respectively, and the integer ambiguity number $w_k \in \mathbb{Z}$. Therefore, the parameter estimation problem is underdetermined. In order to get a unique solution more observations may be added to the model, e.g. by making use of more than two SAR images of the scene, or a priori information may be introduced, e.g. by making certain assumptions about the unknown parameters.

For *topographic mapping* it is usually assumed that (1) no deformation in slant-range direction occured over the data acquisition interval and (2) atmospheric effects can be neglected. Both may for instance be justified if the two SAR images are acquired simultaneously (single-pass interferometry, cf. Figure 4) or if the SAR images are selected carefully. Then, the observation equation (10) reduces to

$$\psi_k = -\kappa \frac{B_{\perp,k}}{r_k \cdot \sin\bar{\theta}_k} \cdot z_k - 2\pi \cdot w_k. \tag{11}$$

Provided that the integer ambiguities w_k have been solved succesfully, equation (11) provides the topographic height for every pixel.

For *deformation studies* the contribution of topography to the interferometric phase has to be modelled and removed; this requires information about the topography. This information may be either a high-resolution digital terrain model or a third or even fourth radar image of the scene. The former is referred to as *two-pass* InSAR, the latter *three-pass* and *four-pass* (differential) InSAR, respectively. If a digital elevation model of the terrain is available the first term on the right-hand side of equation (10) can be computed.

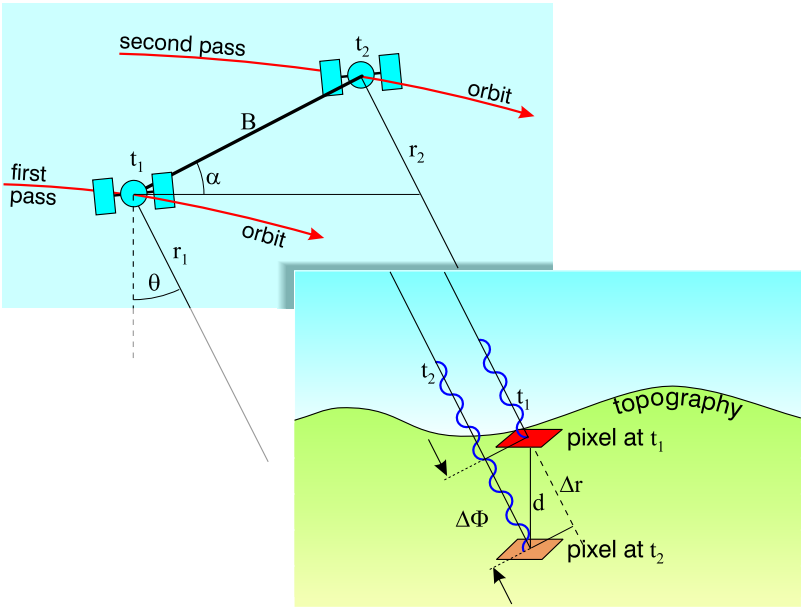

Figure 8: Two-pass InSAR for deformation monitoring. In order to extract the phase $\Delta\Phi$ caused by a deformation between image acquisition at t_1 and t_2, the contribution of topography to the interferometric phase has to be eliminated. This requires a digital elevation model to be available.

Three-pass interferometry uses three SAR images, acquired at time epochs $t_i : i = 1, 2, 3$ to form two interferograms: interferogram I, making use of the SAR images acquired at t_1 and t_2, and interferogram II, making use of the SAR images acquired at time epoch, say, t_1 and t_3. Assuming that interferogram I has succesfully been unwrapped, and no significant deformation occured during the time interval between t_1 and t_2, one may estimate the topography from interferogram I, which is called the *topography pair*, according to

$$z_k = \left(-\Phi_{k,I} + \kappa S_{k,t_1} - \kappa S_{k,t_2}\right) \cdot \frac{r_{k,I} \cdot \sin\bar{\theta}_{k,I}}{\kappa B_{\perp,k,I}}.$$

When inserting this equation into the observation equation for the second interferogram, the *deformation pair*,

$$\psi_{k,II} = -\kappa \frac{B_{\perp,k,II}}{r_{k,II} \cdot \sin\bar{\theta}_{k,II}} \cdot z_{k,II} + \kappa \Delta r_{k,II} + \kappa S_{k,t_1} - \kappa S_{k,t_3} - 2\pi \cdot w_{k,II},$$

one obtains

$$\psi_{k,II} = -b_k \Phi_{k,I} + \kappa(1 - b_k) S_{k,t_1} + \kappa b_k S_{k,t_2} - \kappa S_{k,t_3} + \kappa \Delta r_{k,II} - 2\pi \cdot w_{k,II},$$

where $b_k \approx \frac{B_{\perp,k,II}}{B_{\perp,k,I}}$ denotes the baseline ratio. If no suitable SAR images are available to form the topographic pair, one may also use another suitable interferogram to extract the information about the topography. This is called *four-pass (differential) InSAR*. Assuming that interferogram I formed by images acquired at time epoch t_1 and t_2 is the

topographic pair, the following observation equation is obtained in order to extract the deformation signal:

$$\psi_{k,II} = -b_k\Phi_{k,I} - \kappa b_k(S_{k,t_1} - S_{k,t_2}) + \kappa S_{k,t_3} - \kappa S_{k,t_4} + \kappa d_{k,II} - 2\pi \cdot w_{k,II}.$$

It is important to note that the baseline scaling factor b_k affects the atmospheric contribution. Usually, the *topographic pair* is chosen to have a large baseline (i.e. small b_k) in order to increase the sensitivity w.r.t. topography. Correspondingly, the *deformation pair*, interferogram II, is chosen to have a small baseline, in order to make it less sensitive w.r.t. residual errors in the topographic information, extracted from interferogram I. A zero-baseline deformation pair would make the topographic pair superfluous, and would have normal, i.e. non-scaled, atmospheric contributions. In practise, other factors may influence the choice of the topographic pair as well, such as relief, vegetation, temporal decorrelation and atmospheric conditions. Moreover, the baseline cannot be chosen arbitrarily large, see Section 4 for more details.

Neglecting the atmospheric terms and assuming the phase unwrapping was succesful, the fundamental equation for deformation monitoring using three-pass or four-pass InSAR is obtained:

$$\Delta r_{k,II} = \frac{1}{\kappa}\big(\Phi_{k,II} - b_k\Phi_{k,I}\big), \qquad b_k = \frac{B_{\perp,k,II}}{B_{\perp,k,I}}.$$

Some remarks concerning this equation should be made (Dixon, 1995):

1. The phase difference provides only the line-of-sight component of the three-dimensional surface displacement vector. When using images of both the ascending and descending passes of the satellite, it is possible to extract two components, since, then, the two interferograms represent views of the same scene taken in two different directions.

2. A phase comparison of the two images cannot be done in all cases but depends on the nature of the change. For instance, random motions of the scatterers within a pixel introduce noise in the measured phase difference. When the rms motion exceeds the radar wavelength (typically some centimeters), the noise may exceed the signal, meaning that a pixel-by-pixel phase comparison between the two images is not possible. However, if the entire surface within a pixel moves in the same way, while the relative motion of the elementary scatterers is small compared to the radar wavelength, the information on the deformation can be extracted from the phase difference.

3. The radar-scattering characteristics within each pixel must not change strongly over the time interval the images are acquired. Only then, the unknown phase shift Φ_{scat}, which is caused by the interaction of the electromagnetic wave with the ground, is constant over the time interval $[t_1, t_3]$, and drops out when forming the phase difference. When this condition is not met, it is termed *temporal decorrelation*. It constitutes one of the major problems for InSAR. Vegetation, wind effects, soil moisture,

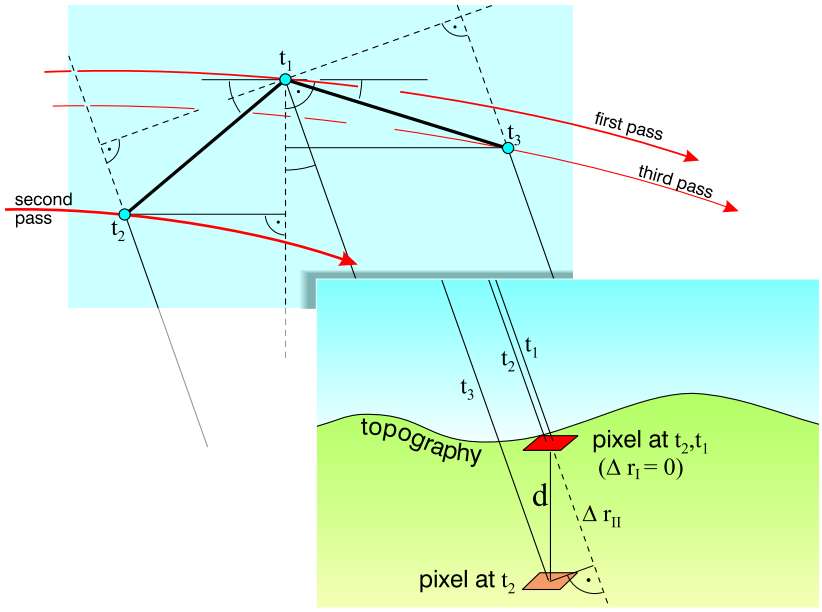

Figure 9: Three-pass SAR interferometry. Images acquired at t_1 and t_2 form interferogram I, which is used to determine the topography ('topographic pair'). Images acquired at t_1 and t_3 form interferogram II, which is used to determine the line-of-sight deformation component Δr ('deformation pair'). Note that a deformation Δr_I in time interval $[t_1, t_2]$ cannot be separated from a deformation Δr_{II} in time interval $[t_1, t_3]$. Only the sum of both can be inferred from the interferometric phase. Therefore, images at t_1 and t_2 are usually selected such that Δr_I can be neglected.

snow fall, farming activities etc. may preclude or hamper the phase comparison of the two SAR images.

4. As mentioned before, one can measure the total interferometric phase Φ only modulo 2π. Therefore, a proper interpretation of the deformation field requires that the interferometric phase has to be unwrapped pixel by pixel. The problem of phase unwrapping is comparable to the problem of ambiguity estimation in GPS phase measurements. Phase unwrapping is a rather difficult step that depends, e.g., on the imaging geometry, the terrain, and the phase noise level. Phase unwrapping is not addressed in these lecture notes; the interested reader may consult e.g. Ghiglia and Pritt (1998). Note also that if no digital elevation model is available, and two image pairs are used to extract the target displacement, a phase unwrapping of each of the two interferograms is mandatory, unless an appropriate integer combination of the interferograms drastically reduces the topographic contribution.

5. Not any arbitrarily large displacement can be detected with InSAR. There are some limits w.r.t. the displacement gradient and the spatial scale of the deformation process, see Section 5 for more details.

6. Measuring the surface displacement field as a fraction of the radar wavelength, i.e.,

to some millimeter accuracy, requires a priori information about the topography in the region. Since the topography may be poorly known, the question arises how sensitive the interferometric phase Φ is to topography? Simple calculations show that a topographic height error of σ_z meters in the digital elevation model will produce an interferometric phase error of $\frac{\sigma_z}{z_{2\pi}}$, where the height ambiguity $z_{2\pi}$ is given by equation (8). Typical errors in digital elevation models are between 10 and 30 meters. Using the nominal ERS SAR parameters $\lambda = 5.66$ cm, $r = 850$ km, $\theta = 23°$, and assuming a perpendicular baseline of $B_\perp = 100$ meters, which gives a height ambiguity of $z_{2\pi} = 94$ meters, phase errors between 0.1 and 0.3 cycles are obtained, which is equivalent to errors in the line-of-sight component of deformation between 3 and 9 millimeters. Since the contribution of topographic errors to the interferometric phase errors grows inversely proportional to the height ambiguity and proportional to the perpendicular baseline $B_\perp$, image pairs with short perpendicular baselines (large height ambiguity) should be preferred to reduce the effect of the unmodeled topography on the deformation.

4 Stochastic model

The major limiting factors for topographic mapping and deformation monitoring using InSAR are (1) the limited measurement accuracy of the interferometric phase (phase noise), (2) the accuracy of the imaging geometry (orbit errors), and (3) the variation in the wave propagation conditions over the data acquisition period (atmospheric signal). In this Section the three major limiting factors are briefly discussed. For more details the reader should consult (Bamler and Hartl, 1998) and (Hanssen, 2001).

4.1 Phase noise

Figure 10 shows the height error as function of the phase noise for various perpendicular baselines. The height error is determined by the perpendicular baseline length and the phase noise. For $B_\perp = 200$ meters a height error of about $\sigma_z = 0.13$ meters per degree of phase error is obtained. Phase errors in the order of 40° result in about 5 meter height errors. The smaller the perpendicular baseline the larger the height error. The phase noise statistic is determined by the response of a resolution cell to the radar pulse, which in turn depends on the scattering mechanism. Two scattering mechanisms are of interest in InSAR: distributed scattering (Gaussian or Rayleigh scattering) and point scattering.

For SAR systems a resolution cell is many wavelengths long in the slant range direction, hereby introducing a very large range of total phase shifts. When folded into the principal interval $[-\pi, \pi)$ this results in a uniformly distributed phase from $-\pi$ to π. Furthermore, it is assumed that no single scatterer dominates the others in a resolution cell, that the phases of the individual scatterers are uncorrelated, and that the amplitude and phase of every scatterer are uncorrelated. Then, the central limit theorem applies and the SAR image pixel is a complex circular Gaussian random variable. For resolutions of tens of

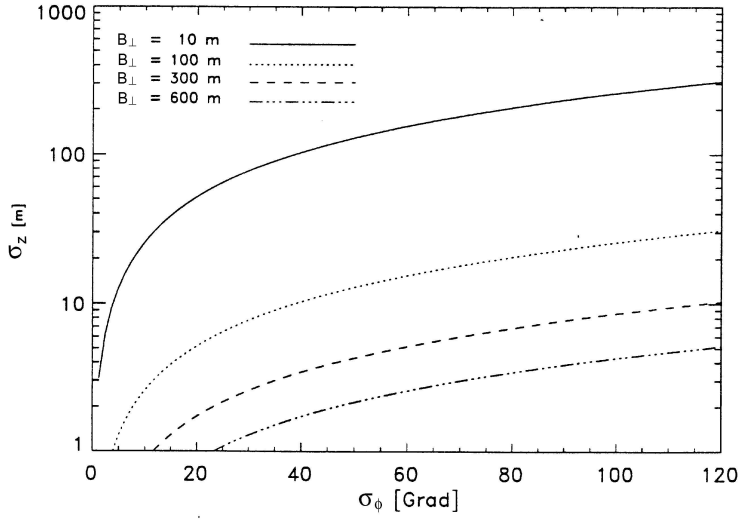

Figure 10: Height error σ_z as function of phase noise σ_ϕ for various perpendicular baselines $B_\perp$.

meters the Gaussian assumption is true for many natural scatterers such as forests, agricultural fields, soil and rock surfaces (Bamler and Hartl, 1998).

For distributed scattering, a pixel in a complex image may therefore be represented as the product of the scattering characteristics and the geometry, hence

$$U = W \exp\left(-\frac{4\pi}{\lambda} r\right),$$

where W is a complex circular Gaussian random variable. The probability density function (pdf) of W, expressed as the joint pdf of its real and imaginary components is

$$pdf(W) = pdf(Re(W), Im(W)) = \frac{1}{2\pi\sigma^2} \exp\left\{-\frac{Re^2(W) + Im^2(W)}{2\sigma^2}\right\}.$$

That means, the real component $Re(W)$ and the imaginary component $Im(W)$ are Gaussian distributed with the same variance σ^2. When expressed as the joint pdf of its amplitude A and phase ϕ, the pdf of W is

$$pdf(A, \phi) = \begin{cases} \frac{A}{2\pi\sigma^2} \exp(-\frac{A^2}{2\sigma^2}) & \text{for } A \geq 0 \text{ and } -\pi \leq \phi < \pi \\ 0 & \text{otherwise} \end{cases}.$$

The marginal probability density function of A and ϕ are then

$$pdf(A) = \begin{cases} \frac{A}{\sigma^2} \exp(-\frac{A^2}{2\sigma^2}) & \text{for } A \geq 0 \\ 0 & \text{otherwise} \end{cases},$$

and

$$pdf\,(\phi) = \begin{cases} \frac{1}{2\pi} & \text{for } -\pi \leq \phi < \pi \\ 0 & \text{otherwise} \end{cases},$$

respectively. That is, the amplitude A is Rayleigh distributed and the phase ϕ is uniformly distributed over $[-\pi, \pi)$. The latter implies that there is no information in the phase of a single SAR image pixel of a Gaussian scatterer due to the summation over many scatterers of random phase. Moreover, phase and amplitude are uncorrelated.

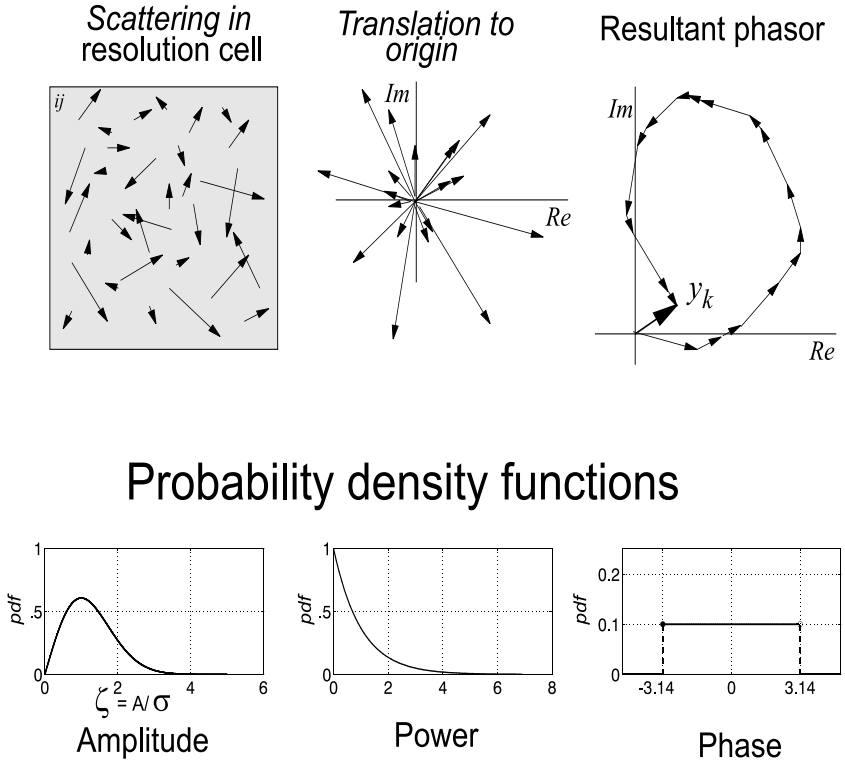

Figure 11: Single pixel scattering statistics (from Hanssen, 2001). Top panels from left to right: The distribution of many individual phasors within a resolution cell; all phasors translated to the same origin (scaled); the phasor sum of all scatterers. The fat arrow indicates the (scaled) sum, which is the complex observable. Bottom panels from left to right: Probability density functions for amplitude, power, and phase. Note that the phase of the radar data is uniformly distributed.

A complex interferogram is formed as product of one complex SAR image with the complex conjugate of a second. A pixel in the interferogram is thus

$$V = U_1 U_2^* = W_1 W_2^* \exp\left(-\frac{4\pi}{\lambda}(r_1 - r_2)\right),$$

with

$$W_1 W_2^* = A_1 A_2 \exp\left(i\,\delta\phi\right),$$

where $\delta\phi = \Phi_{1,scat} - \Phi_{2,scat}$. The joint pdf of W_1 and W_2 can be written as

$$pdf\,(W_1, W_2) = \frac{1}{\pi^2 |C|} \exp\left(-(W_1^*, W_2^*) C^{-1} (W_1, W_2)^T\right),$$

where C is the complex covariance matrix, defined by

$$C = E\{(W_1, W_2)^T (W_1^*, W_2^*)\} = \begin{pmatrix} E\{|W_1|^2\} & \gamma\sqrt{E\{|W_1|^2\}E\{|W_2|^2\}} \\ \gamma^*\sqrt{E\{|W_1|^2\}E\{|W_2|^2\}} & E\{|W_2|^2\} \end{pmatrix}.$$

γ is called the complex correlation coefficient or *coherence* of the two SAR images:

$$\gamma = \frac{E\{W_1 W_2^*\}}{\sqrt{E\{|W_1|^2\} \cdot E\{|W_2|^2\}}} = |\gamma| \exp(i\tilde{\Phi}).$$

Its phase $\tilde{\Phi}$ is the expected interferometric phase, i.e. the desired noise-free phase used for topographic mapping and deformation monitoring. Its magnitude $|\gamma|$ is a measure of phase noise. From the joint pdf of magnitude and phase of an *interferogram sample* $w_1 \cdot w_2^*$ the marginal pdf of the interferometric phase Φ is computed:

$$pdf\,(\Phi) = \frac{1 - |\gamma|^2}{2\pi} \frac{1}{1 - \beta^2} \cdot \left(1 + \frac{\beta \cdot \arccos(-\beta)}{\sqrt{1 - \beta^2}}\right),$$

with $\beta = |\gamma| \cos(\Phi - \tilde{\Phi})$. Thus, the marginal pdf of the interferometric phase is fully characterized by $\tilde{\Phi}$ and $|\gamma|$. When restricting phase values to an interval $[\tilde{\Phi} - \pi, \tilde{\Phi} + \pi)$ then the mean and variance of the phase are

$$E\{\Phi\} = \tilde{\Phi},$$
$$\sigma_\Phi^2 = \frac{\pi^2}{3} - \pi \arcsin|\gamma| + \arcsin^2|\gamma| - \frac{1}{2}\sum_{k=1}^{\infty} \frac{|\gamma|^{2k}}{k^2},$$

respectively. When examining the shape of the phase pdf for different coherence values $|\gamma|$ it is observed that the phase is nearly uniformly distributed for $|\gamma| = 0$, i.e. it carries no information at all. In the limit of the noiseless case ($|\gamma| = 1$) the pdf degenerates to a $\delta-$function centered at $\tilde{\Phi}$. Obviously, the coherence γ governs the statistics of interferograms of Gaussian scatterers. Under ideal conditions, SAR imaging is a deterministic process, i.e. identical imaging conditions yield the same result. Under real conditions, a number of disturbances occur, which degrade the coherence (decorrelation). The reasons are

- thermal noise within the radar system (γ_{SNR})
- errors induced by the SAR processing (γ_{proc})
- temporal variations of the backscatter (γ_{scene})

- different observation geometries at the two data acquisitions (γ_{geom})

As a result, the coherence γ can be written as the product of various terms,

$$\gamma = \gamma_{SNR} \cdot \gamma_{proc} \cdot \gamma_{scene} \cdot \gamma_{geom}.$$

For instance, γ_{scene} stands for the temporal scene coherence and is defined as the ratio of temporarily stable scattering contributions to the total scattering intensity transferred to the SAR images. If the two SAR images have been acquired at different times, the structure of the scatterers may have changed in the meantime. The contribution γ_{geom} is the geometric decorrelation, caused by a the perpendicular baseline $B_\perp$. It causes a shift of the two image spectra. If this shift exceeds the system bandwidth, it results in complete loss of correlation. Therefore, there is a maximum perpendicular baseline, which never must be exceeded. For ERS-satellites this is about 1.1 km for flat terrein. In practice no ERS SAR-image pairs with perpendicular baselines larger than 600 m should be used due to the increased noise level.

4.2 Orbit errors

The extraction of topography and deformation from interferograms and the proper referencing of topopgraphic and deformation maps to a specific coordinate system require information about the satellite coordinates during the few seconds of SAR image acquisition. As along-track errors are usually corrected for during the coregistration of the SAR images only radial and across-track errors propagate into the interferogram. Estimated radial and across-track errors in the ERS orbits provided by the Delft Institute for Earth-Oriented Space Research (DEOS) are on the order of 5 cm and 8 cm, respectively. The orbit errors result in a residual interferometric phase, which can be erroneously interpreted as topography or deformation. The orbit-error induced fringe pattern depends on the orientation of the baseline error vector, which cannot be predicted. As an example, Figure 13 shows the maximum residual fringes in an 100×100 kilometers interferogram as function of the radial and across-track errors. One fringe or less corresponds to rms values of 5 and 10 centimeters residual fringes in the interferogram. Expected maximum rms values are 80 and 160 centimeters in radial and across-track direction. In practice tie points distributed over the scene may be used to correct for the orbit error induced fringe pattern in the interferogram. At least 4 tie points with different known heights are necessary in order to solve for the baseline error vector. Practical problems with tie points may happen if the interferogram is corrupted by atmospheric signal. In addition, long-wavelength fringe patterns may also be caused by a deformation process or by errors in the topographic model, and this signal would be attributed to the orbit error when the latter is estimated using tie points. Finally, if the interferogram suffers from decorrelation, it may be difficult to identify a long-wavelength phase pattern, which is typical for orbit errors, and to attribute it to orbit errors.

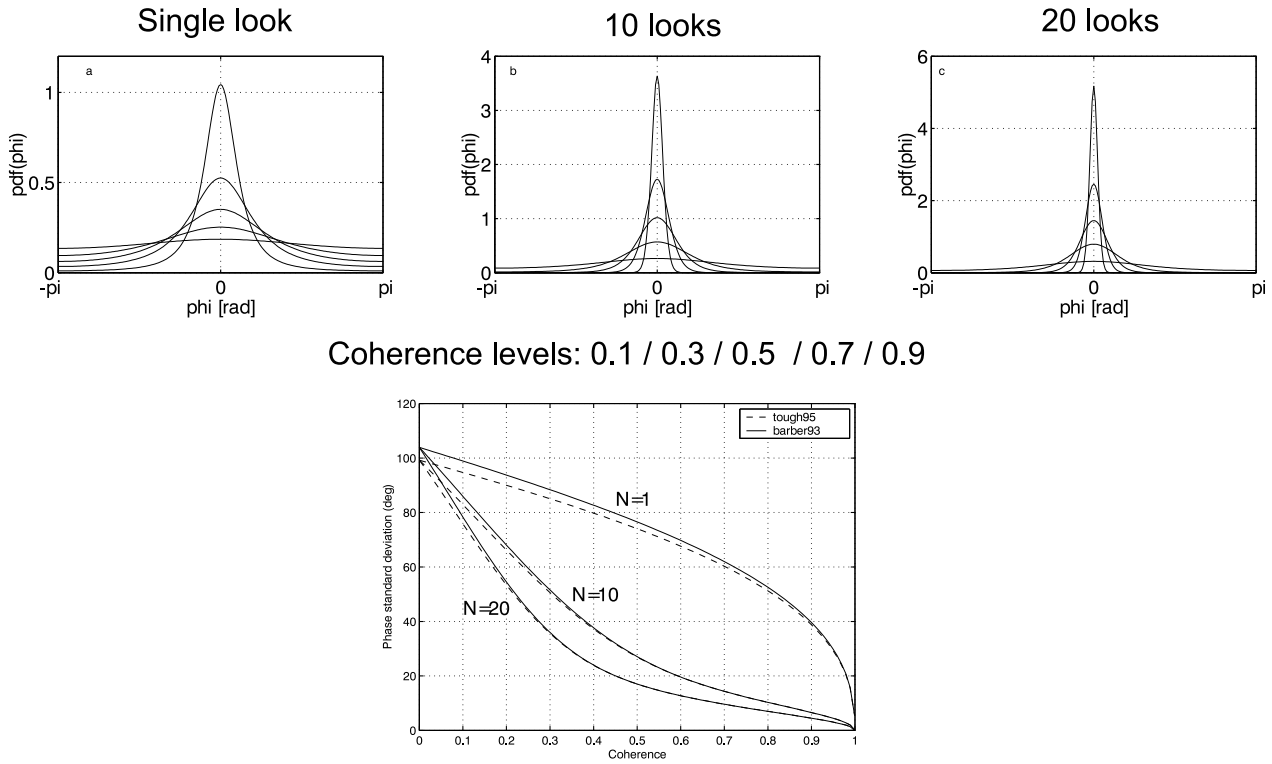

Figure 12: Interferometric phase statistics (from Hanssen, 2001). Top panel: Probability density functions for coherence levels $|\gamma| = 0.1,\ 0.3,\ 0.5,\ 0.7$, and 0.9 (narrow curves correspond with higher coherence). From left to right: single look, multilook level 10, multilook level 20. Multilooking means that the average of a number of pixels is taken; this improves the phase statistics. Bottom panel: Standard deviation of the interferometric phase as function of coherence for three multilook levels.

The effect of (residual) orbit errors on topography can be described by (cf. (11))

$$dz = -\frac{dB_\perp}{B_\perp} \cdot z,$$

where $dB_\perp$ is the perpendicular baseline error. Thus, the (perpendicular component of the) baseline error results in an erroneous scaling of the topographic height with factor $\frac{dB_\perp}{B_\perp}$. For instance, in order to map a mountain with an elevation of 1000 meters with an accuracy of about 1 meter the relative accuracy in the perpendicular baseline must be better than 10^{-3}. If the error is, say, $dB_\perp = 0.20$ meters, a perpendicular baseline of $B_\perp > 200$ meters is needed.

4.3 Atmospheric path delay

The determination of surface changes using InSAR is based on the assumption that the radar signal propagates unaffected in the atmosphere. This, however, is not the case. Path delays occur in both the ionosphere and the troposphere. Ionospheric path delay is

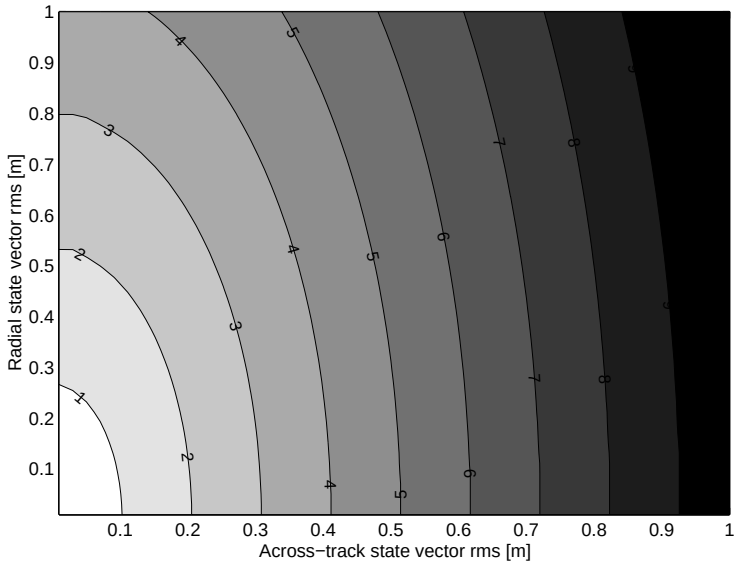

Figure 13: Maximum amount of residual fringes in an interferogram as a function of the radial and across-track state vector accuracies. With a 95% confidence, the maximum number of fringes is less then shown here (from Hanssen, 2001).

caused by variations in the Total Electron Content (TEC) along the path and by Traveling Ionospheric Disturbances (TID). The former depends on the time of day and influences the whole scene rather homogeneously. The latter, however, can be significant for InSAR scenes, since it may cause localized artifacts.

The most severe atmospheric effect is due to the troposphere. Its path delay consists of two components, a dry part (about 2.3 meters in vertical direction) and a small but highly variable wet part. The latter is dominated by the strong temporal and spatial variability of the water vapor concentration. It can take on magnitudes up to 30 centimeters.

Artifacts in interferograms have been reported quite often and some of them have been assigned to atmospheric perturbations. These effects can cause misinterpretation of deformation fields derived by InSAR in the order of centimeters. For instance, a differential interferometry chart of the Kilauea volcano system, generated by data of the April and October mission of SIR-C in 1994 was interpreted firstly as a demonstration of a volcanic lift of several centimeters, but turned out later to be just an atmospheric effect as was reported by a JPL team on several occasions. Especially in wet regions SAR images exhibit artifacts due to the temporal and spatial variations of atmospheric water vapor. Other tropospheric variations, such as pressure and temperature, as well as ionospheric perturbations induce distortions as well, but the effects are smaller in magnitude and more evenly distributed throughout the interferogram than the wet tropospheric term.

Figure 14 shows the strong signature of precipitating cumulonimbus clouds as a local-

ized delay difference in the SAR line-of-sight caused by a cloud and the saturated sub-cloud layer. The line-of-sight delay differences have been mapped to differences in zenith-integrated precipitable water, the vertically integrated water vapor liquid equivalent using a simple cosine mapping function. The positive sign of the delay indicates that the feature appeared in the first of the two combined SAR images. The interferogram also shows phase variations over areas with no precipitation, which suggests that water vapor gradients are seen in the interferogram that are not observable by a weather radar. The right panel of figure 14 shows the height differences obtained if the atmospheric signal is interpreted as topographic signal ($B_\perp$ = 80 meters). Height differences of up to 300 meters appear although the area is completely flat, due to the erroneous interpretation of phase variations caused by the precipitating cumulus cloud.

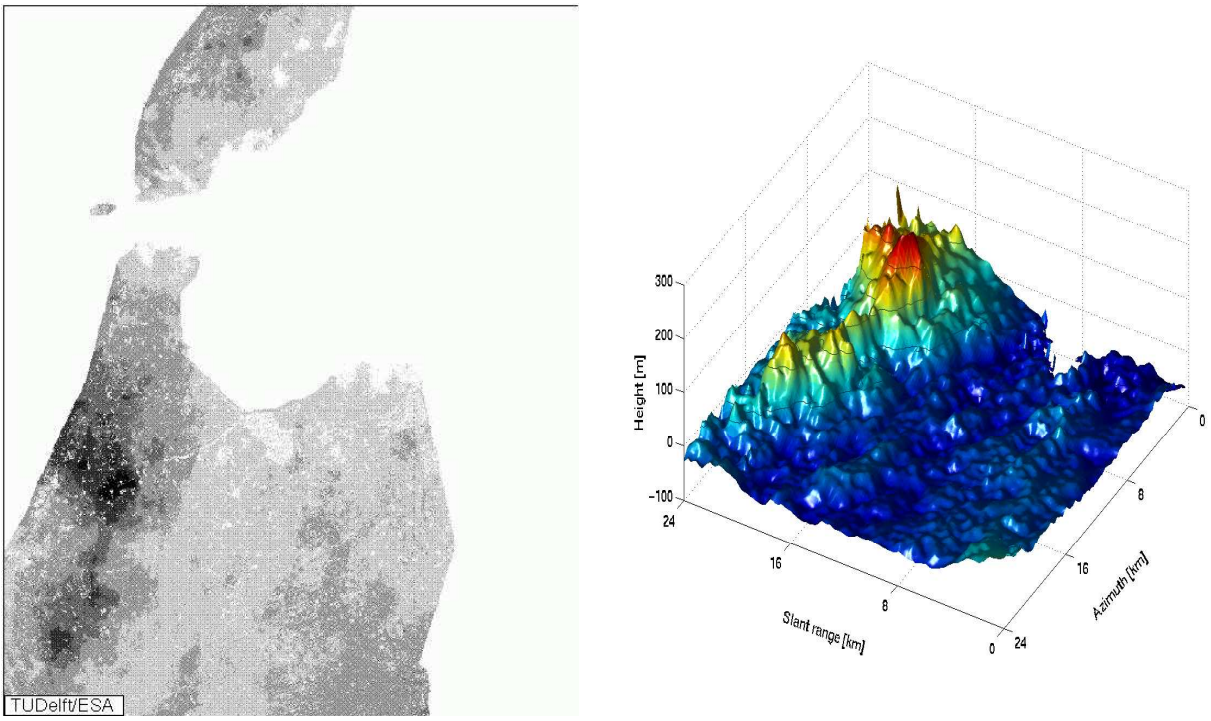

Figure 14: Interferometric signature of precipitation. Left panel: the SAR interferogram (29 and 30 August 1995) shows slant delay variations, mapped to zenith-integrated precipitable water differences. The average of the undisturbed area is set to zero, yielding relative precipitable water estimates. Right panel: slant delay variations mapped into topographic heights ($B_\perp$ = 80 meters). The area is approximately 25 × 25 kilometers (from Hanssen et al. 1999).

Figure 15 shows an interferogram of the area of Groningen, The Netherlands. The images have been acquired during the ERS-1/2 tandem mission on two successive days and show the fringe pattern, which is due to convective cells. More than 4.5 fringes corresponding to a line-of-sight path delay of 12.6 centimeters can be counted showing that atmospheric effects can have a very large influence on the interferogram. Since these effects are inde-

pendent of frequency at microwave wavelengths, the contamination of the signal cannot be mitigated by dual-frequency measurements such as those commonly utilized for ionospheric corrections.

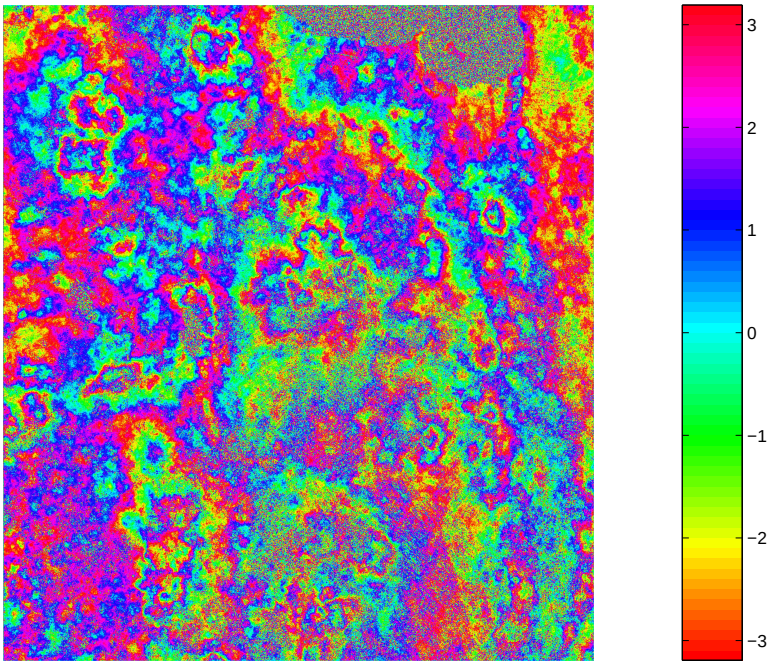

Figure 15: Interferogram of the Groningen area taken over one day. The fringe patterns indicate the influence of convective cells during the data acquisition. Up to 4.5 fringes corresponding to 12.6 centimeters line-of-sight propagation delay can be counted (from Hanssen, 1998).

Not only lateral variation in refractivity can cause atmospheric artefacts in SAR interferograms. Also vertical stratification, which is the result of different vertical refractivity profiles during the two SAR acquisitions, may lead to significant distortions in mountainous areas. Figure 16 shows a sketch of two different vertical refractivity profiles and their effect on two points p and q on an imaginary mountain. The panel on the right of Figure 16 shows the cumulative delay of the rays to p and q. The observed delay between the two points in the interferogram due to the vertical stratification is equal to $l_2 - l_1$, i.e. the observed phase error in the interferogram between p and q is only due to the difference in the cumulative delay values at both altitudes. Note that it is not possible to calculate this phase error using surface meteo data, since the whole refractivity profile is needed. For instance, a cloud layer in between p and q would not be noticed in the surface meteo data, whereas it could shift the cumulative delay noticeable, as indicated by the dotted line. To study the variability of the refractivity 365 radio sonde profiles acquired at noon during 1998 in the Netherlands have been analyzed. The refractivity values or delay values in ppm are shown in Figure 17. Using this data set it is possible to derive the delay differences between 2 points for every height interval. The 2σ-values

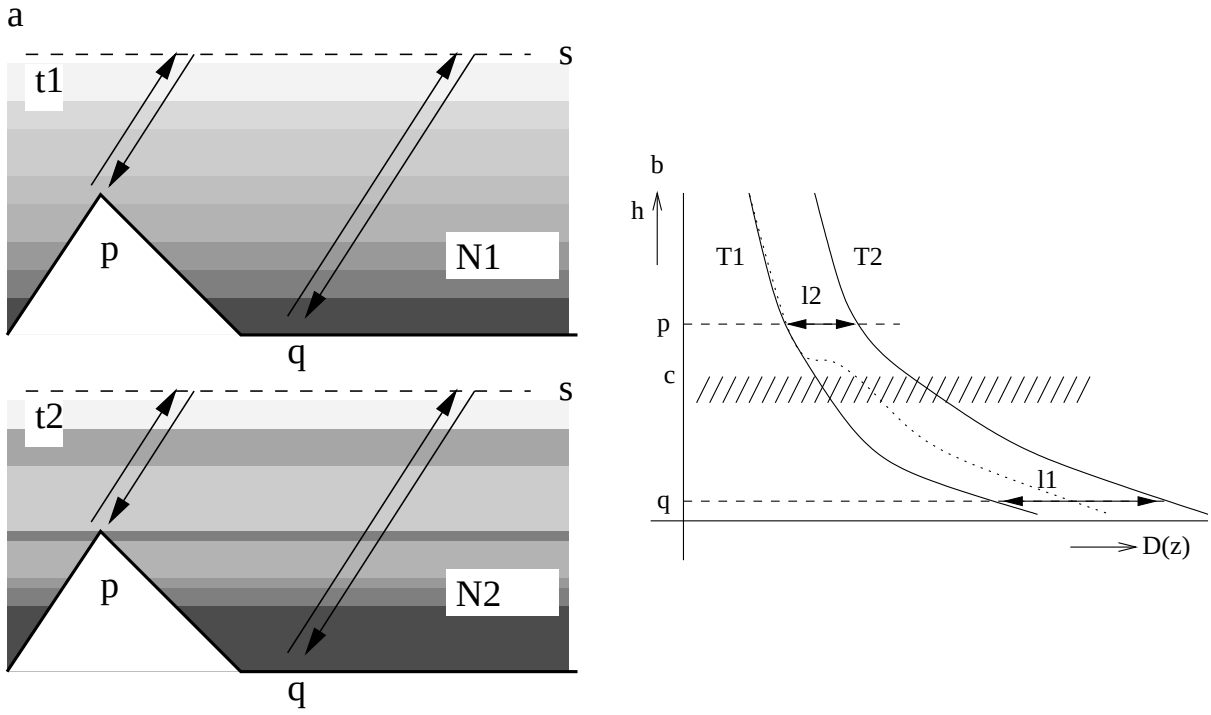

Figure 16: Left panel: Differential tropospheric delay between point p at the top and point q at the foot of a mountain due to a different vertical refractivity profile during the two SAR acquisitions at time t_1 and t_2. Right panel: The cumulative delay curves for t_1 and t_2 indicating the height of points p and q. The effect of the delay on the interferometric phase difference between p and q is determined only by the difference $l_2 - l_1$. The presence of for instance an extra cloud layer c at t_1, indicated by the dashed area, will cause a shift of the cumulative delay profile below the cloud, indicated by the dotted line. From (Hanssen, 2001).

and worst case values for a 1-day interval and a 182-day interval are shown in Figure 18. With an accuracy of better than $2-3$ mm the following empirical formula is found for the standard deviation of the interferometric phase due to differential tropospheric layering as function of the time interval between the two data acquisitions and the height difference between two points:

$$\sigma_\varphi = \frac{4\pi}{\lambda}\frac{1}{\cos\theta}\big(33.7 + 0.08\Delta t\big)\sin\frac{z\pi}{2z_s}$$

for $1 \leq \Delta t \leq 182$ and $0 \leq z \leq z_s$. Δt is the time interval in days, z represents the height in meters and $z_s = 5000$ m is a scale height. Above this height, the variability of the refractivity is considered negligible.

Turbulent mixing is another even more general form of atmospheric disturbance, which affects all types of space-geodetic radio observations (VLBI, GPS, radar altimetry, InSAR). On short spatial scales the dominant signal is caused especially by water vapor variability. Figure 19 shows the power law behavior of the turbulent signal. A $-8/3$-exponent is

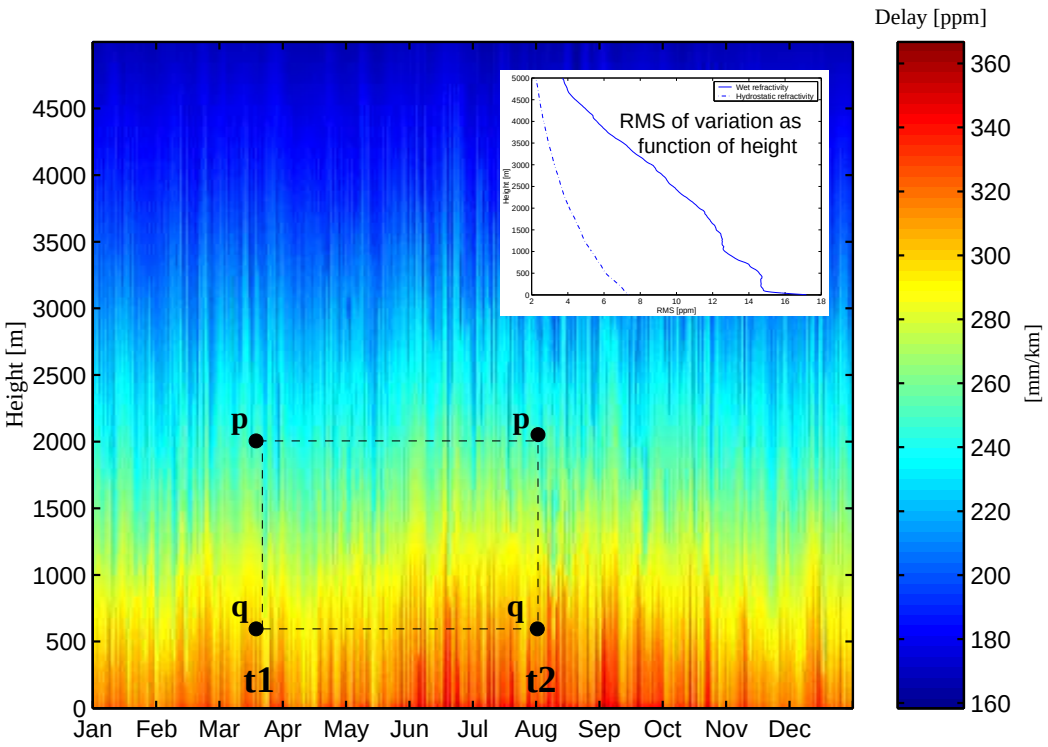

Figure 17: Refractivity or fractional delay in ppm for 365 radiosonde observations acquired at noon in 1998. The inset shows the variation of refractivity as function of height. The unpredictable wet part of the refractivity accounts for most of the variability.

observed over wavelengths smaller than the effective height of the troposphere, say $2-3$ kilometers. For larger wavelengths, a $-5/3$-exponent is observed. The insets of Figure 19 show the corresponding differential interferograms. The power spectra are obtained using a rotational average over the 2D-spectra. The variance of phase difference measurements over a fixed spatial interval is found using the structure functions shown in Figure 20, defined by

$$D_\varphi(R) = E\{[\varphi(x+R) - \varphi(x)]^2\}.$$

$D_\varphi(R)$ can be used to derive the covariance function:

$$Cov(i,j) = \frac{1}{2}\big(D_\varphi(\infty) - D_\varphi(R)\big).$$

Expanding the covariance function for all the combinations of pixel i and j yields the variance-covariance matrix as shown in Figure 21. The covariance matrix has a Block Töplitz-Töplitz Block (BTTB) structure. For these matrices, fast inversion techniques exist.

Ideally, atmospheric signal needs to be included in the mathematical model for applications of repeat-pass InSAR. As long as no perpendicular means are available to obtain

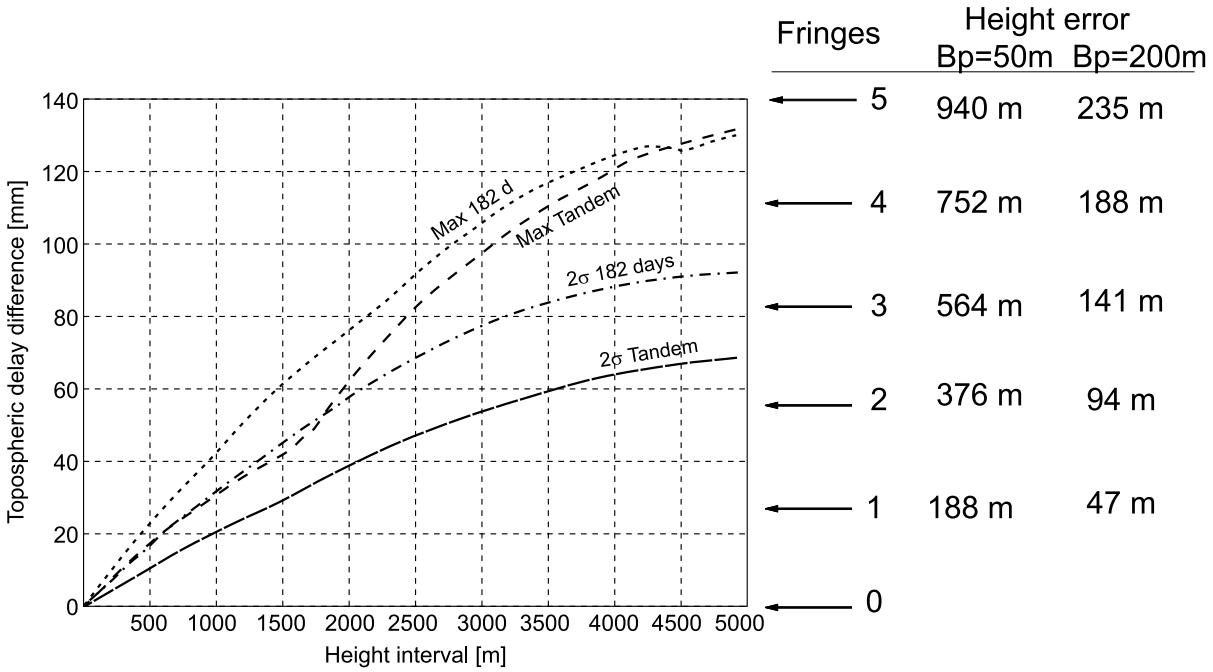

Figure 18: Errors due to vertical stratification. *Bp* means *perpendicular baseline*. The curve '2σ Tandem' indicates the expected tropospheric delay difference as function of height difference for a SAR image pair of the ERS Tandem mission (temporal baseline 1 day); the curve '2σ 182 days' the corresponding delay for a temporal baseline of 182 days. The two curves denoted by 'max' indicate the expected maximum delay. For instance, for a height difference of 1500 m the 2σ rms of the tropospheric delay difference is 30 mm; this corresponds to an interferometric phase signature of about 1 fringe, which maps into a height error of 188 m for a perpendicular baseline of $B_\perp = 50$ m and of 47 m for a perpendicular baseline of $B_\perp = 47$ m.

quantitative information with sufficient spatial resolution, high accuracy, and at the time of SAR data acquisition, the atmospheric signal will deteriorate the quality of the topographic or deformation maps. In that case the atmospheric distortions should at least be described stochastically and be included into the stochastic model of InSAR in order to obtain more realistic error estimates for InSAR-derived products.

5 Applications

Since the launch of ESA's ERS-1 in 1991 many applications of InSAR have been developed. Thematic applications exploit the information about the coherence together with backscatter and texture. This information is used for instance for land classification, forest management, soil moisture monitoring, and flooding monitoring. Geometric applications exploit in particular the information about the phase in the radar echo, which is used in order to extract the topographic signal, the deformation signal or the atmospheric signal in SAR interferograms. Only the application for deformation monitoring will be discussed, because it is the most exiting field of applications due to the potential of InSAR

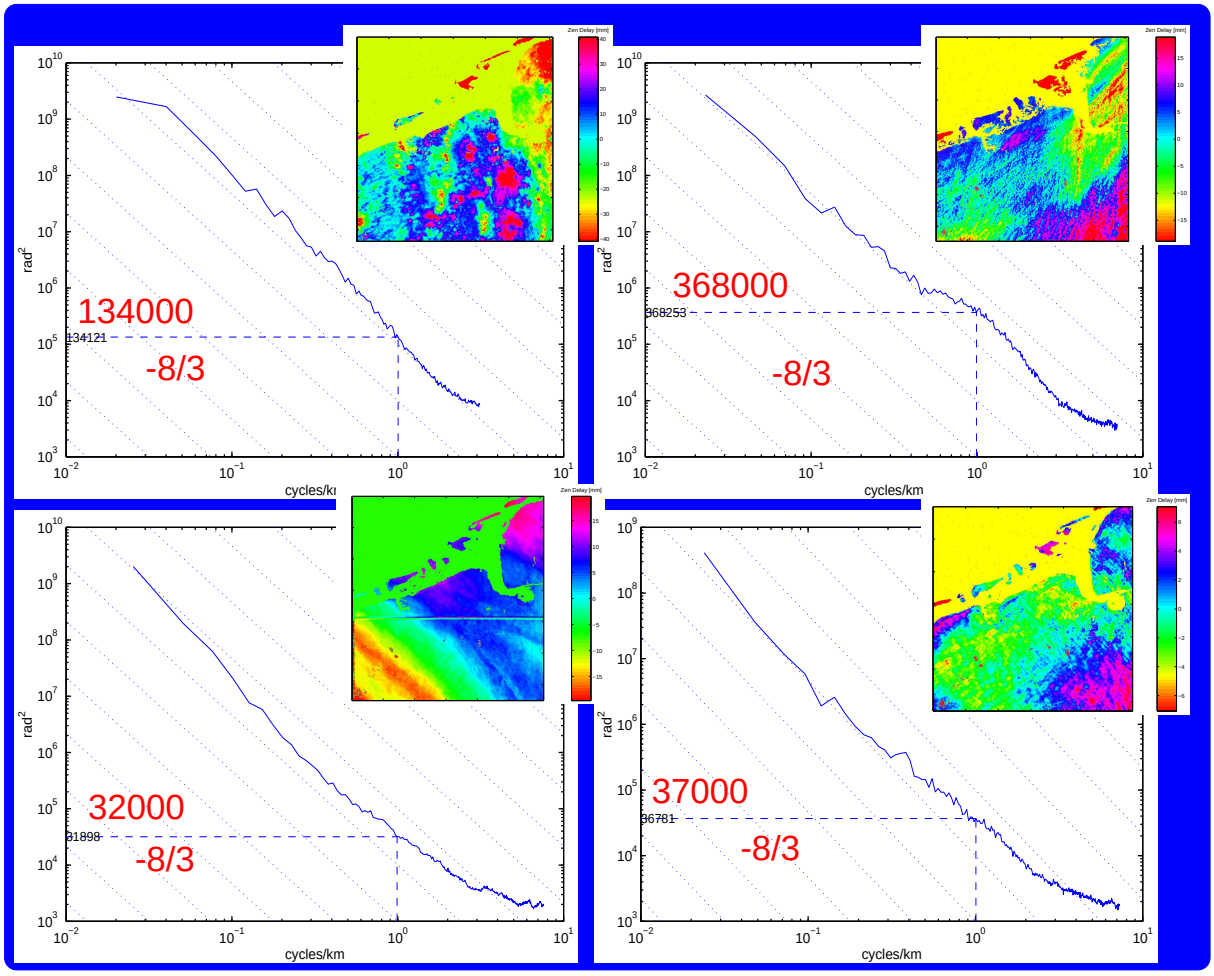

Figure 19: Atmospheric power spectra of four arbitrary interferograms (see insets) acquired over the northern part of the Netherlands.

to map centimeter-scale ground displacements over a region many tens of kilometers in size at a resolution of a few meters.

InSAR may be applied to all kinds of deformation processes: land subsidence caused by withdrawal of ground water, oil or gas, co- and postseismic deformations, volcano deformation, and glaciers and ice sheet kinematics. One could even think of monitoring man-made objects like dams. Before presenting some examples it should be noted that the spatial dimensions of detectable deformation signals are limited by several parameters (cf. Figure 22):

1. *The pixel size and swath width bounds:* physical limitations on the spatial wavelength of the deformation signal that can be measured. Signals with spatial wavelengths smaller than the image pixel or much larger than the size of an image scene cannot be detected by InSAR alone.

2. *Upper and lower limits of the deformation gradient:* these bounds are set by the criteria of 1 fringe per pixel and 1 fringe per scene. For ERS 1/2 each fringe represents

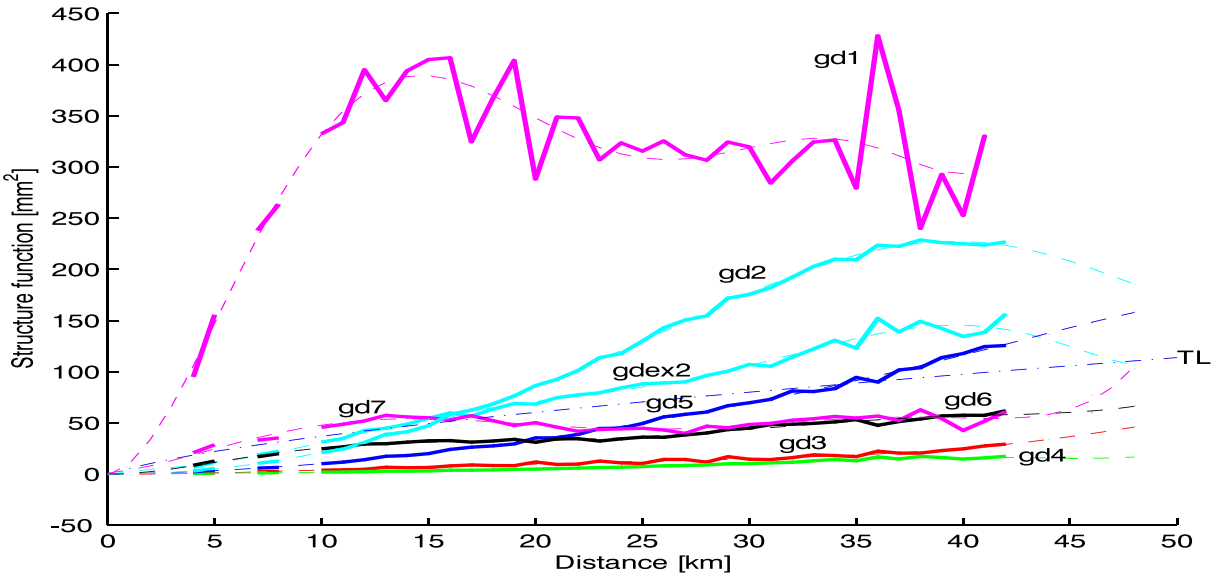

Figure 20: Structure functions of eight 'atmospheric' interferograms denoted by gd1,...,gd7, and gdex2. The structure function expresses the variance of a spatial difference.

28 mm LOS displacement, the resolution is approximately 20 m, and the swath width is 100 km giving approximate bounds of 10^{-3} on the steepest displacement gradient and 10^{-7} on the shallowest displacement gradient detectable by InSAR.

3. *Phase and atmospheric noise level:* they limit the smallest LOS displacement signal that can be measured at any spatial wavelength. Phase noise prohibit the measurement of signals smaller than a few mm. Atmospheric noise is spatially variable and can have magnitudes of up to 12 cm. It does not prohibit the measurement of the signal but can contaminate it significantly leaving the interpretation open to argument.

5.1 Earthquake Research

An earthquake has provided the first full scale validation of InSAR as a geodetic technique. The ground deformation of the Landers earthquake, which ruptured the surface up to 6 meters and shook southern California on June 28, 1992 with a magnitude 7.3, has been observed using two-pass InSAR (Massonnet et al. 1993), and has triggered a wealth of other studies, cf. for instance the review papers (Massonnet and Feigl, 1998) and (Klees and Massonnet, 1999). Since then, many earthquakes have been analyzed using various satellites and, sometimes, SAR images acquired by various satellites are used providing more insight into the role of InSAR in earthquake-related studies.

Figure 23 shows an interferogram of the western portion of the North Anatolian fault zone in Turkey. This area was struck by a Mw 7.4 earthquake on 17 August 1999, which

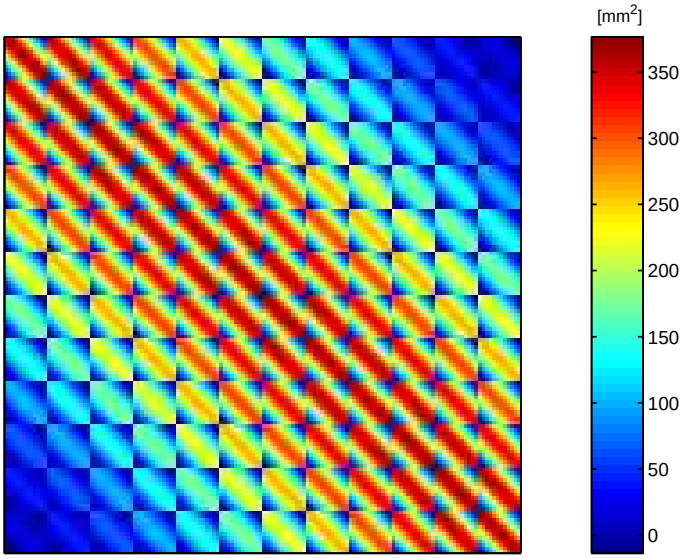

Figure 21: Variance-covariance matrix obtained for the vectorized observations derived from the empirical structure function. A 12×12 interferogram is assumed with a pixel size of 0.16 km. The matrix exhibits a Block Töplitz-Töplitz Block (BTTB) structure. From (Hanssen, 2001).

ruptured the surface over about 130 kilometers length along the North Anatolian fault. The slip on the fault was almost parallel to the Earth's surface, and the fault plane was almost vertical. This results in predominantly horizontal deformations along the fault, almost exactly in the look direction of the SAR. The maximum horizontal displacement measured in the field was about 5 meters. The interferogram results from two ERS-2 SAR images acquired at 13 August 1999 and 17 September 1999. The topographic signal has not been removed but contributes at most by one fringe to the interferogram due to the large height ambiguity. Therefore, the interferometric fringes show more or less the horizontal motion along the North Anatolian Fault. One run through the colour wheel corresponds to 28 millimeters line-of-sight deformation, which is equivalent to about 72 millimeters horizontal movement. Note that the interferogram only shows relative deformations between any two points in the interferogram. If the complete scene had moved one would not observe any interferometric phase pattern, and thus, could not detect this movement. For instance, about 27 fringes line-of-sight deformation are counted from the southern coast of the Black Sea to the Gulf of Izmit, which is equivalent to 1950 millimeters ground movement. This indicates that the Northern coast of the Gulf of Izmit has moved away from the radar relative to the Southern coast of the Black Sea by about that distance. In reality, the deformation was even larger, since in the vicinity of the fault no clear fringe pattern can be detected anymore. This is due to the large deformation gradient in the vicinity of the fault and the effect of temporal decorrelation, both show up as noisy areas in the interferogram. Note also that the deformations on both sides of the fault are not connected to each other. This could be done for instance using GPS tie

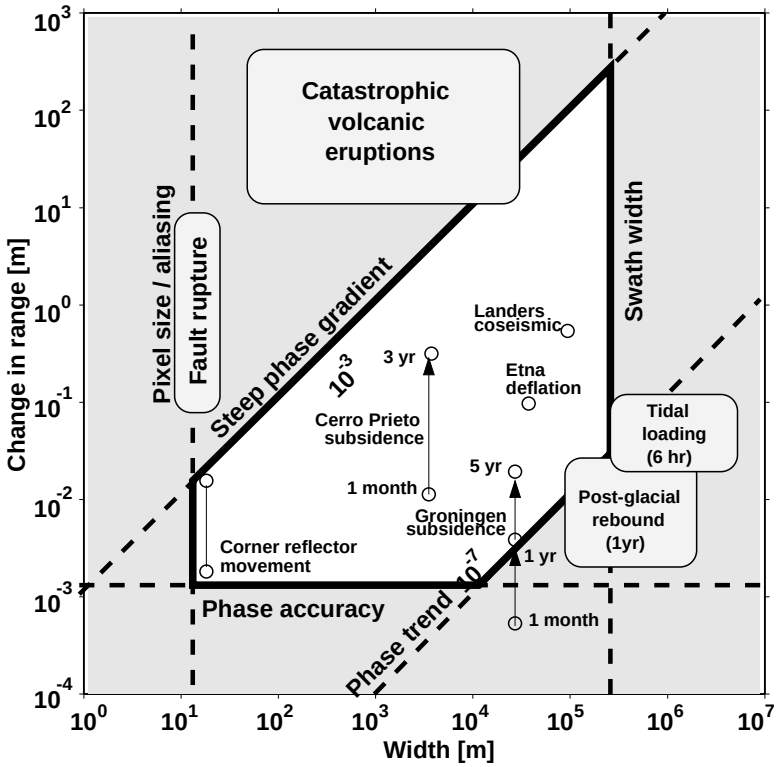

Figure 22: Limitations of measuring deformations of the Earth's surface using InSAR (Hanssen, 2001, modified from Massonnet and Feigl, 1998).

points on both sides of the fault.

One of the important geophysical questions related to earthquakes is that of stress relaxation which is a key parameter in order to assess the likelihood of future seismic hazard. It is known that the seismicity rate increases in regions of stress increase and falls where off-fault stress decreases. Areas without stress relaxation can be identified in the Izmit interferogram by converging fringes indicating no relative motion between the Eurasian Plate to the North and the Anatolian Plate to the South. This seems to be the case around the Gulf of Izmit. This would indicate that the Izmit earthquake increased the stress beyond the west end of the rupture (similar to the east end, not shown here), which may trigger future earthquakes in these areas. However, computations of the stress transfer rely heavily on reliable determinations of the fault geometry and the slip gradient, which can be estimated using InSAR, or even better, using a combination of various satellite techniques such as GPS, InSAR and SPOT.

A crucial point in the wide acceptance of InSAR by the geophysical community was the similarity of the interferometric result with a synthetic interferogram build from the surface rupture measurement assuming an elastic behavior of the crust. The Landers example was perfectly pedagogical in the sense it did not show totally unexpected results on a large scale while giving surprisingly accurate results on secondary phenomena, such

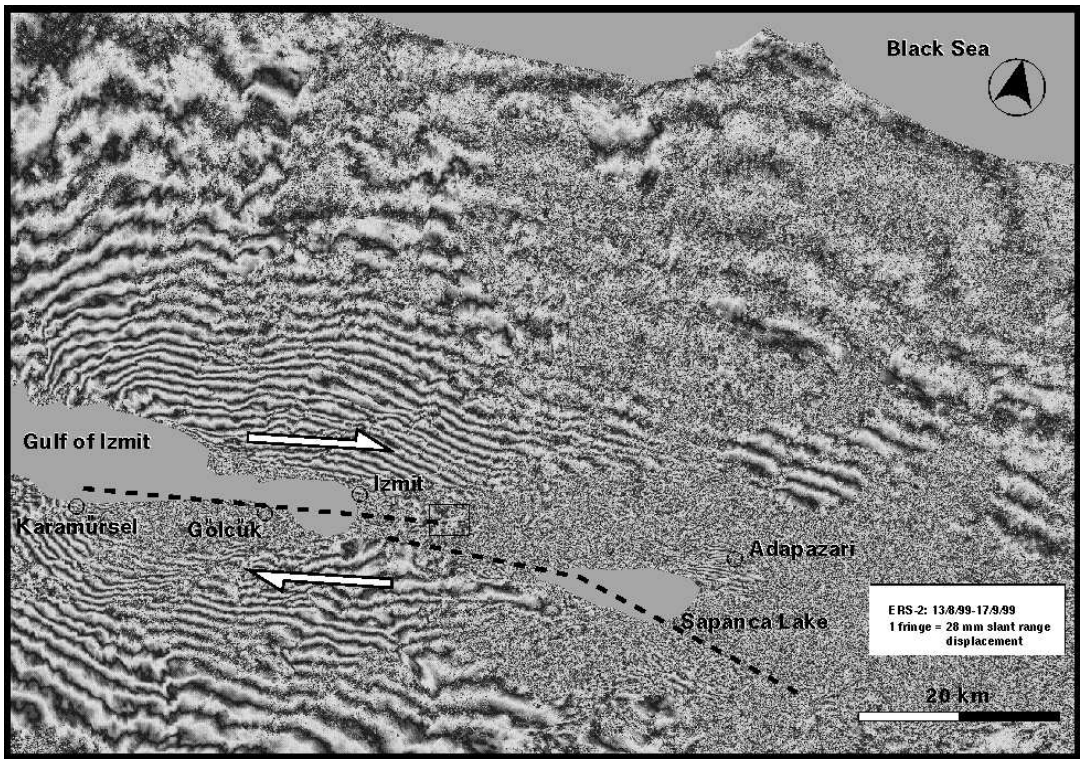

Figure 23: Deformation field of the Mw 7.4 earthquake on 17 August 1999 along the North Anatolian fault zone near Izmit, Turkey, mapped by InSAR.

as tiny fault shifts triggered by the main shock. Often these shifts have not been detected by GPS and terrestrial geodetic measurement techniques. Similar holds for other features like surface deformation patterns associated with individual aftershocks and surface offsets, features that would be very difficult, if not impossible, to detect on the ground. Often (but not always, as the Izmit earthquake shows) InSAR is able to map the complex, near-fault patterns of post-seismic deformations unambiguously while GPS would need an impossibly dense and costly network of stations. While InSAR agrees with GPS measures, the latter has difficulties deciding between various geophysical models of the earthquake mechanism because of the strong spatial undersampling of the deformation field. Fault models based on GPS measurements may fail to account for significant parts of the fringe patterns observed by InSAR for the co-seismic deformation fields. This can be attributed to the low number of fault parameters estimable from the GPS measurements due to the poor spatial sampling of the GPS networks. InSAR, however, allows the estimation of a more detailed fault model, thus providing a better fit to the data than the GPS derived models.

So far, no precursory displacements (assuming that they exist!) have been detected in SAR interferograms. In addition, loss of coherence may prevent mapping deformations very near the fault trace as the Izmit earthquake has shown. Finally, it may happen that the earthquake does not create clear interferometric fringes. Only co-seismic deformation

fields with sufficient magnitude and proper orientation w.r.t. the look direction of the radar sensor can be mapped. Mostly, moderate (Mw > 5) earthquakes at shallow depth ($<$ 10 kilometers) with predominantly vertical or horizontal surface displacements generate fringes allowing for an unambiguous interpretation.

5.2 Volcano Monitoring

Volcano monitoring using InSAR offers a clear, near term perspective in disaster prevention for several reasons: first of all, many of the world's volcanoes that actually do erupt experience significant pre-eruption surface deformations. Secondly, the position of volcanos is well known and their systematic survey would require only a few hundred local DEM's and a few thousand radar images per year. Thirdly, the deformation is continuous rather than step-wise, and it is associated with a typical time scale of months rather than (many) years. Finally, many volcanoes remain sufficiently coherent although atmospheric distortions, steep topography, vegetation, and snow coverage at summit may cause serious problems. The interested reader should consult the review papers (Zebker et al., 2000) and (Massonnet and Sigmundsson, 2000).

The first interferometric study of a volcano (Massonnet et al., 1995) drew a lot of attention because it revealed unknown features of the deflation of Italy's Mt Etna during the end of one of its last eruptions. New significant results were obtained, namely the unexpected depth of the source of deformation, which was not indicated by classical geodetic techniques. Amelung et al. (1999) conducted a detailed study of a large number of volcanoes from different environments and showed that the application of InSAR for volcano monitoring depends on both viewing geometry and physical conditions. Extreme environmental conditions such as rain, snow, and dense vegetation may cause temporal decorrelation over very short time scales of one day. The viewing geometry together with steep slopes may lead to very high fringe rates, making it difficult or impossible to unwrap the interferograms, thus preventing an unambiguous interpretation of the signals. Moreover, intrusion of magma into the magma chamber prior to an eruption does not necessarily show up as deformation at the surface. The best targets for radar interferometry are obviously basaltic, low-relief shield volcanoes with shallow magma reservoirs and large calderas. Silicic stratovolcanoes with substantial relief and deeper magma reservoirs are often less suited due to large geometric distortions (layover, foreshortening), severe environmental conditions near the summits (snow and ice cover, at least seasonally), and greater vegetation cover, resulting in a loss of coherence. Future satellite missions, however, could be designed to optimize volcano study: using greater incidence angles would reduce the problem with geometric distortions related to steep topography, and the use of longer wavelengths such as L-band (24 centimeters) lessens the issue of temporal decorrelation.

Figure 24 shows a time series of deformations over various periods of the area of the Phlegrean Fields caldera located in the Neapolitan area in Italy, derived from InSAR (Usai et

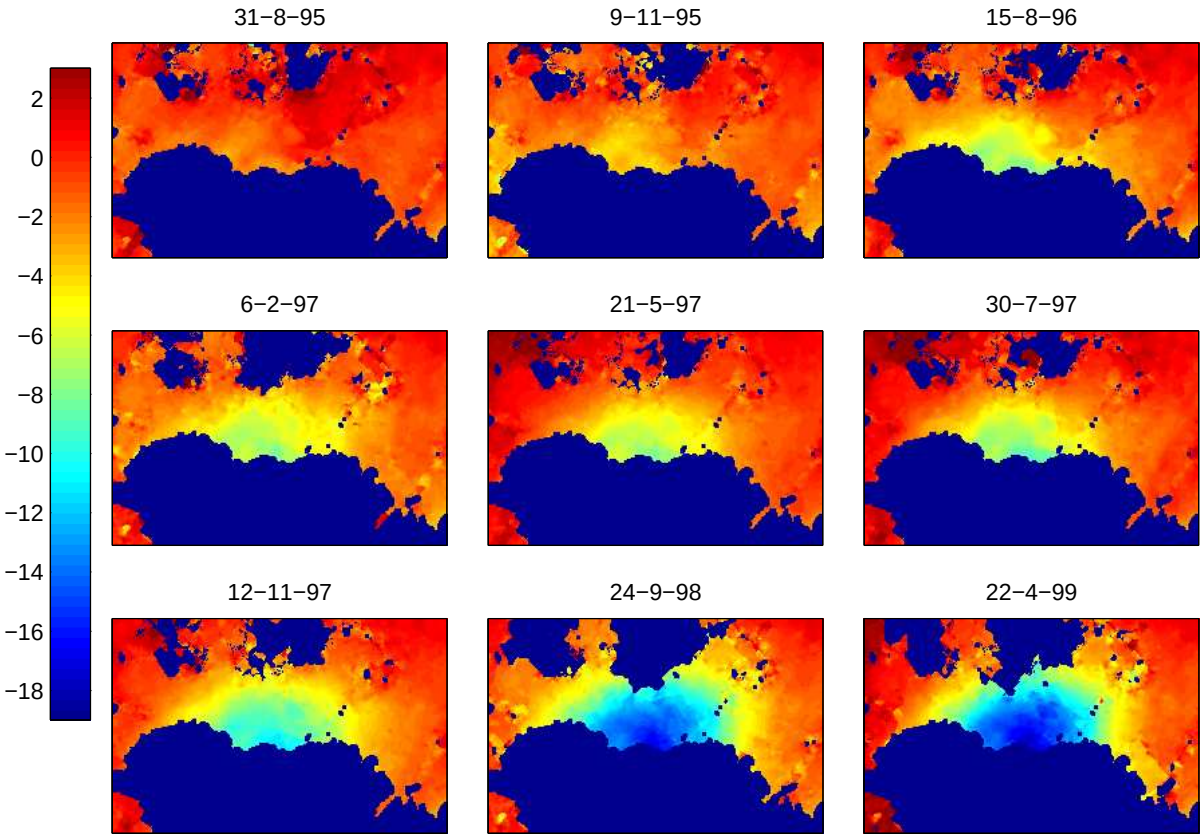

Figure 24: Time series of deformations (cm) of the Phlegrean Fields caldera since 12 April 1995 mapped by InSAR. From (Usai et al. 1999).

al., 1999). The area is located near Mt. Vesuvius and is subject to strong volcanic activity. Strong vertical displacements have been observed during periods of seismic activity with ground uplifts up to about 2 meters, followed by slow subsidence with rates of a few centimeters per year. A set of 13 SAR images has been used to compute 21 interferograms spanning different time intervals. Figure 25 shows a SAR interferogram with a temporal baseline of about 1 year. A tandem pair with an perpendicular baseline of $B_\perp = 100$ meters has been used to generate a digital elevation model of the area. The three-pass (differential) InSAR method has been used to extract the deformations. After phase unwrapping and removing a bias in some of the interferograms using leveling data, which may be caused by e.g. phase unwrapping errors a least-squares adjustment was performed with the first day as reference and the deformations relative to the reference day at nine selected days as unknowns. The 9 plots shown in Figure 24 represent the deformation in centimeters at each of the nine days w.r.t. the reference day. By comparison with levelling data, an rms of 4 millimeters has been estimated. The dense spatial sampling gives a complete picture of the deformation of the whole area. The high temporal sampling allows to monitor the evolution of the deformation in time. In particular temporal changes in the deformation rate can be inferred from the time series. For instance, in the period August 1996 to May 1997 the subsidence rate decreased w.r.t. the preceeding period, but

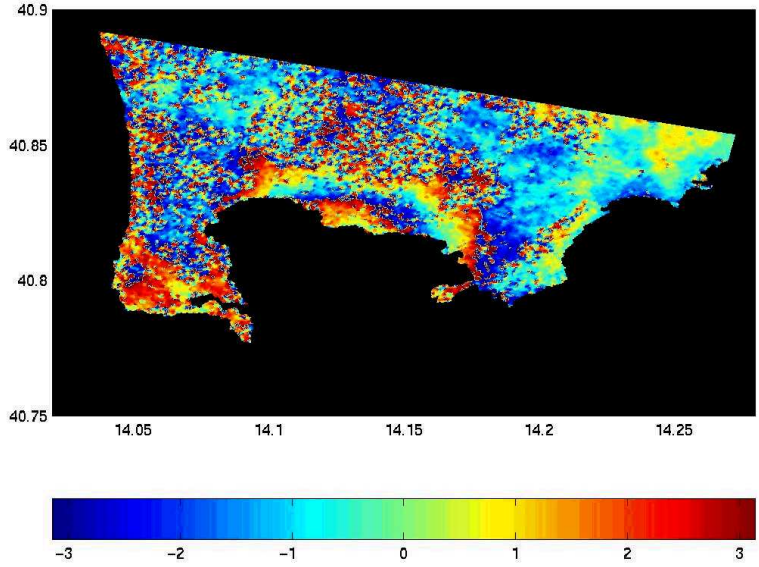

Figure 25: Geocoded interferogram of the Phlegrean Fields caldera from two SAR images acquired at 31 August 1995 and 15 August 1996. One run through the colour bar represents a line-of-sight deformation of 28 mm. From (Usai et al. 1999).

increased slightly from May 1997 to April 1999.

5.3 Anthropogenic Processes

Many man-made activities can generate terrain deformation with the kind of spatial extend and gradient boundaries measurable by InSAR, i.e. an area at least several tens of pixels across is meant with a relative deformation gradient typically lower than 10^{-3}. An example is the effect of material withdrawal, whether solid, like in coal extraction and any kind of deep-mining activity, or fluid, like water used in geothermal plants, for irrigation or underground salt dome washing, and last but not least oil or gas. The terrain may also be deformed by underground explosions, such as in tests of nuclear weapons or in destruction of old mines. Man-made activities do not result exclusively in subsidence: underground gas storage and vapor assisted oil extracted may result in uplift as well. Most of these activities have been mapped by InSAR and more or less openly discussed. As example, the application of InSAR for monitoring land subsidence at the Cerro Prieto geothermal plant will be briefly discussed. For more details the reader should consult (Hanssen, 2001).

The Cerro Prieto geothermal field is located in the Mexicali Valley, 30 km southeast of the city of Mexicali, Baja California in Mexico near the border of California. The field is located in an actively developing rift basin, a region with high seismicity, high heat flow,

Figure 26: Topographic interferogram of the Cerro Prieto area. Perpendicular baseline $B_\perp = 310$ meters, height ambiguity $z_{2\pi} = 30$ meters.

and volcanism. Due to the extraction of water and steam from the geothermal system at depths of $1500 - 4000$ meters, the area suffers from land subsidence on the order of 6 cm/year averaged over the last 35 years with maximum velocities of more than 10 cm/year located in the center of the geothermal field.

In order to analyse the spatial and temporal evolution of this small and quite slow local phenomenon of subsidence a time series of SAR images acquired between April 1995 and August 1997 has been used. The topography was determined from an ERS-tandem image pair with an perpendicular baseline of $B_\perp = 310$ meters and a height ambiguity of about 30 meters. The topographic interferogram was scaled and subtracted from every deformation pair; the resulting differential SAR image pairs were used for deformation monitoring. As deformation pair only acquisitions within a baseline band less than 200 meters are selected in order to make them less sensitive to errors in the topographic model. Figure 26 shows the topographic interferogram. The area is almost flat up to the 225 meters elevated Cerro Prieto volcano to the west of the geothermal plant, corresponding to $7 - 8$ fringes. Figure 5.3 shows four 70-day interferograms. The features marked in the top right and bottom left panel are caused by atmospheric path delay. The SAR image acquired at 16 March 1997, which is common to both interferograms has been identified as being corrupted by atmospheric effects. This becomes clear when forming the sum and the difference of the top right and bottom left interferogram, see Figure 28. The sum removes the atmospheric signal and leaves the pure deformation signal over 140 days (Figure 28 left bottom panel). The difference shows the atmospheric signal two times amplified but no deformation (Figure 28, right bottom panel). The atmospheric signal is

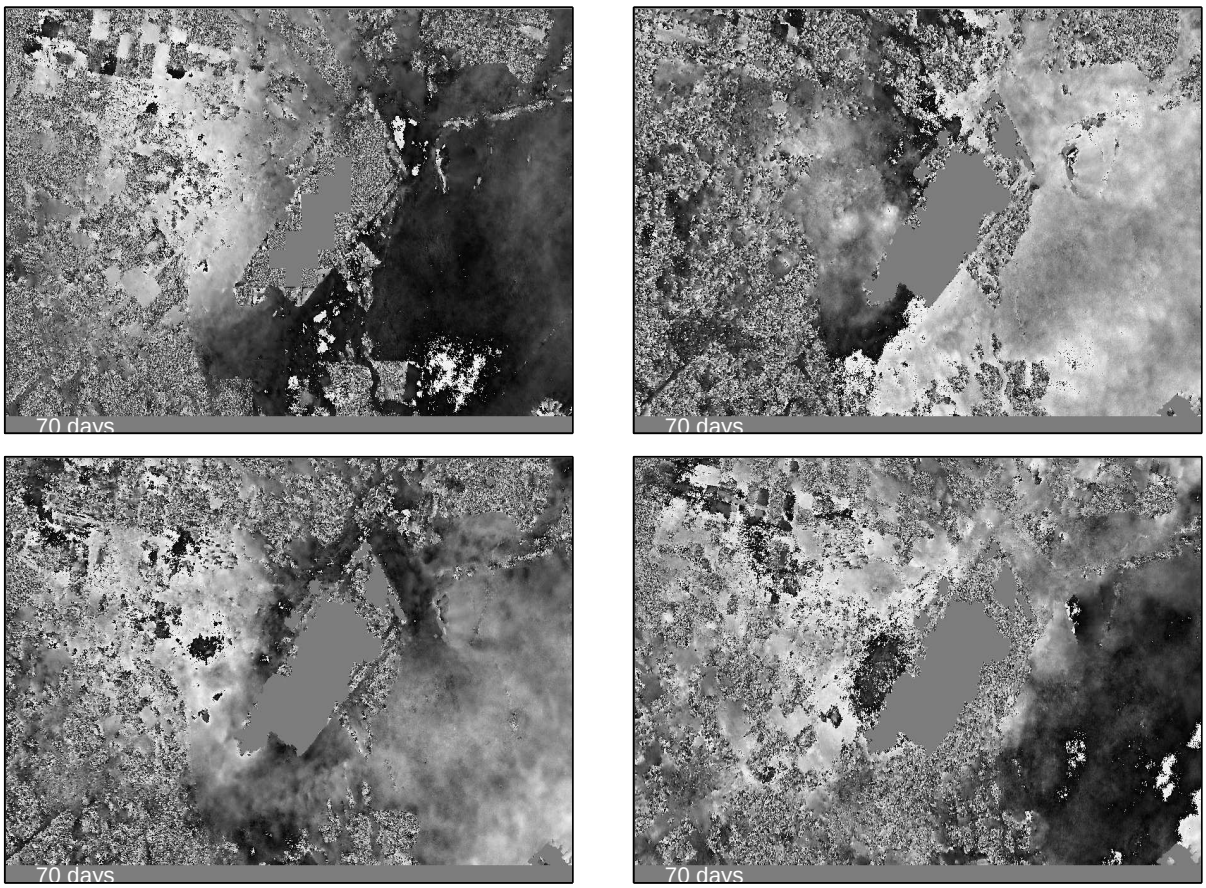

Figure 27: Four 70-day interferograms of the Cerro Prieto area from SAR images acquired between November 1995 and August 1997. The area is about 12×18 kilometers, and contains about 600×900 pixels of approximately 20×20 meters. The deformation pattern, centered over the geothermal plant area is clearly visible. Note the two features marked in the top right and bottom left interferogram, representing atmospheric distortions.

about one fringe corresponding to 28 millimeters line-of-sight deformation. This strategy, which is called *pairwise logic* is often used in order to identify atmospheric distortions in SAR interferograms. It requires, however, that enough suitable SAR images are available in order to form various pairs.

The effect of temporal decorrelation is clearly visible in Figure 29, which shows four interferograms with temporal baselines between 176 days and 491 days. Loss of coherence over longer time spans is mainly caused by agricultural activities in that area and the natural variations of the surface related to seasonal cycles or irrigation. The desert located westwards of the Cerro Prieto field shows a high degree of coherence over years. The implication of the temporal decorrelation is that typically a number of isolated but still sufficiently coherent areas (patches) can be identified, carrying the deformation signal. These high coherence patches are separated by areas of low coherence, which do not

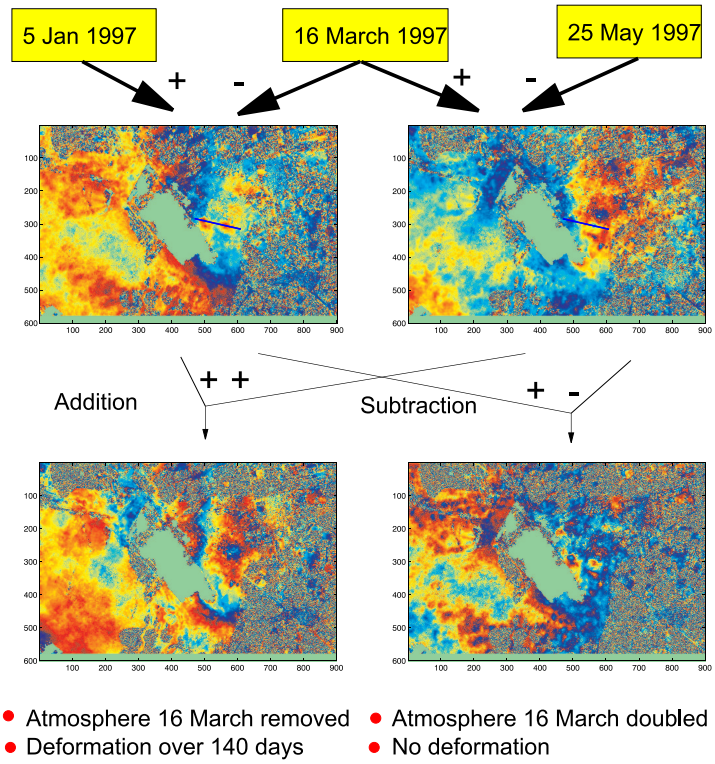

Figure 28: Identification of atmospheric signal by pairwise logic. The SAR image acquired at 16 March 1997 is common to both interferograms. The sum of the two interferograms removes the atmospheric signal of the SAR image acquired at 16 March 1997, the difference doubles the atmospheric signal. This allows to identify the SAR image acquired at 16 March 1997 as corrupted by atmospheric signal.

contain any useful information about the deformation (Figure 30). This makes the unambiguous extraction of the deformation signal from the differential interferograms very difficult due to the ambiguity problem. That is, the phases within each isolated but coherent patch may be unwrapped successfully; but one is left with the problem how to connect the various patches in order to get an unambiguous deformation signal. Under these conditions, the unambiguous extraction of the deformation signal is quite difficult and only possible if a priori information and reasonable assumptions are made. For Cerro Prieto, information about the maximum deformation gradients (from the analysis of some levelling data), the expected long wavelength deformation signal (due to the extreme depths of extraction varying between 1500 and 4000 meters) and the assumption of a constant deformation rate has been used to succesfully unwrap the interferogram, see right panel of Figure 30. The latter assumption, for instance, allows to extrapolate in time the relatively coherent 70-day interferograms, which provided a first guess for the ambiguities between the isolated patches.

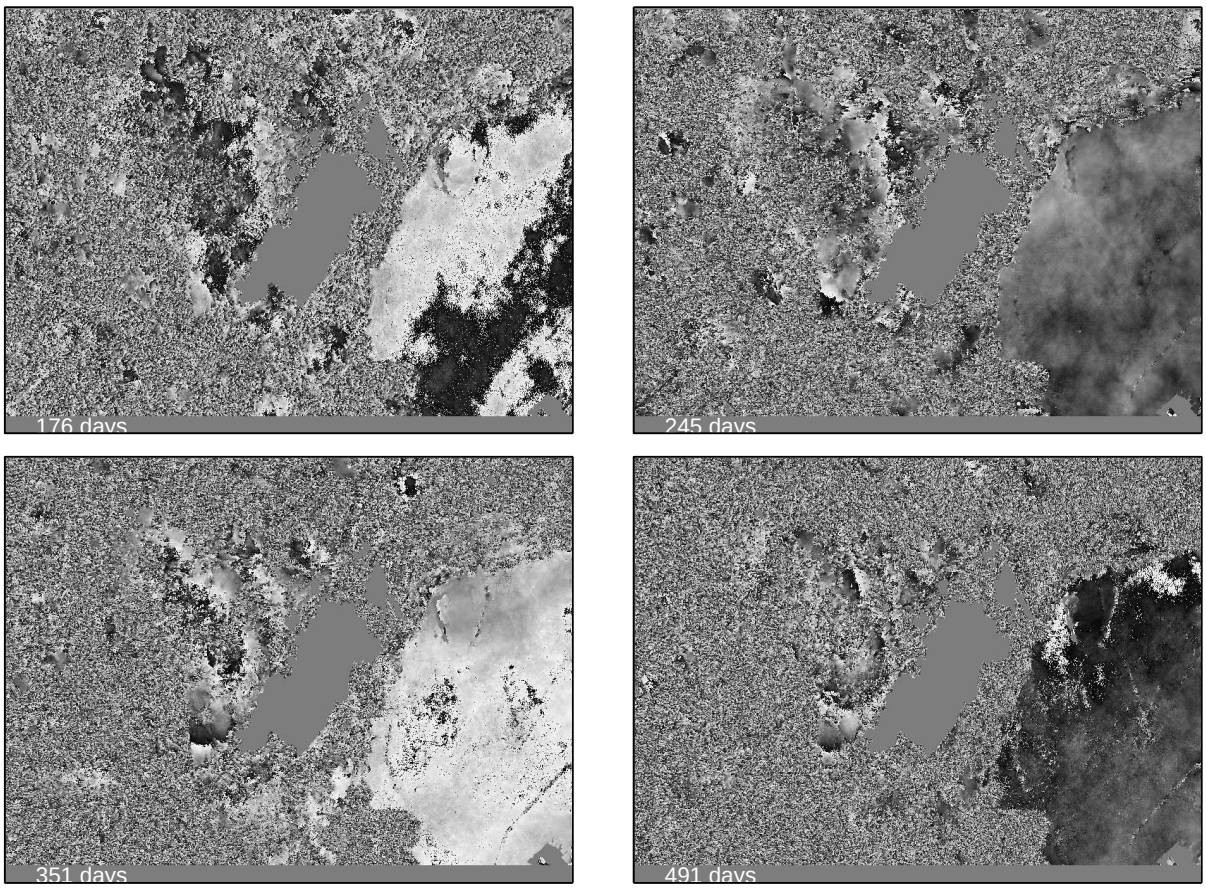

Figure 29: Four interferograms spanning time periods between 176 and 491 days. The deformation signal is clearly visible, although temporal decorrelation due to agricultural activities, seasonal cycle, and irrigation increases considerable.

5.4 Glacier and Ice Sheet Monitoring

With regard to glacier and ice sheet monitoring, recent examples have demonstrated that InSAR can (a) provide high-resolution high-accuracy topographic maps of glaciers and ice sheets, (b) measure ice flow velocity without any ground control, (c) detect and monitor surface changes, (d) identify the line separating floating from grounded ice, and (e) measure changes in surface geophysical parameters.

Figure 31, taken from (Hartl et al. 1994), shows an interferogram of the area around Hemmen Ice Rise on the Filchner-Ronne shelf ice in the Antartic, derived from two ERS-1 SAR images acquired at 26 and 29 January, 1992 during the ERS-1 ice phase. On the right side the western slope of Berkner Island, which rests on bedrock, is seen, and on the left Hemmen Ice Rise grounded on sea-bed shoals and surrounded by the floating Ronne Ice Shelf. The clear fringes of the Ronne Ice Shelf reflect not only the motion of the Filchner-Ronne shelf ice over 3 days, but also the topography and the effect of the differential tides. To distinguish between these effects, further information is needed or

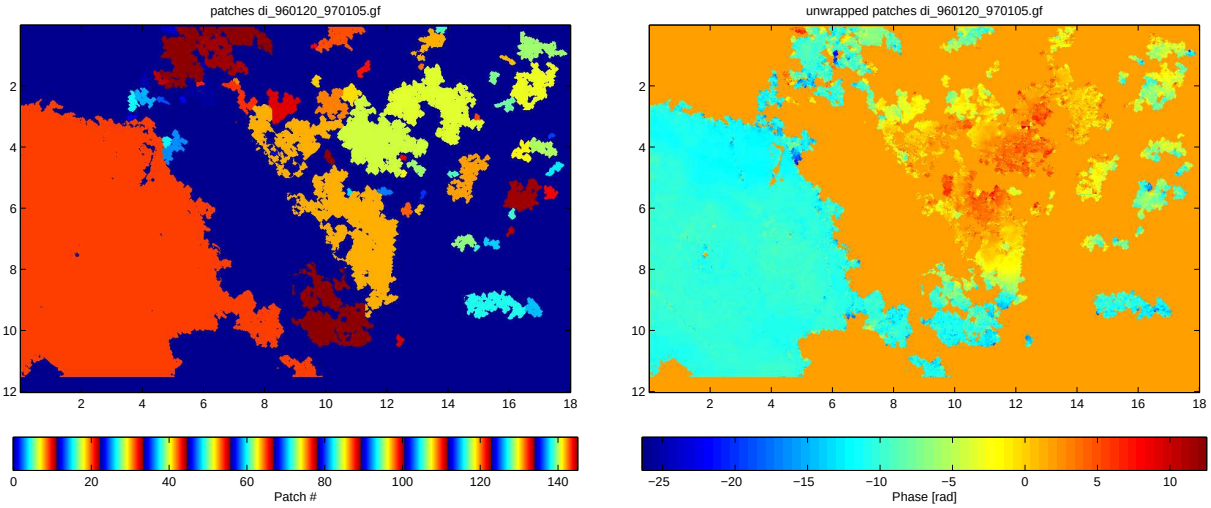

Figure 30: Left panel: 145 isolated but coherent patches have been identified in an interferogram spanning a time period of 351 days. Right panel: unwrapped interferogram.

certain assumptions have to be made. For instance, if one is interested in the tidal signal, three SAR image can be used to form two independent interferograms. Then, assuming that the topography has not changed and the ice flow was steady during the data acquisition times, taking the difference between the two interferograms cancels the effect of steady motion and topography, thus providing the line-of-sight deformation due to tides (cf. Figure 32).

Severe limitations to InSAR for polar and glacier studies come from the temporal decorrelation and the need to separate between various effects that contribute to the fringe pattern such as ice motion, topography, and tides. Changes in snow and ice conditions may yield very noisy interferograms over time scales much shorter than the repeat period of the satellite. Additional problems arise due to the fact that InSAR only measures the line-of-sight component of the velocity vector with reasonable high accuracy and because sometimes it can be difficult to find stationary regions in the scene.

The separation of various effects and the determination of the three-dimensional velocity field normally requires more SAR images. Moreover, the latter is not possible without some assumptions. On the other hand, due to the temporal decorrelation, the number of SAR images needed to infer the required information should be as low as possible. With regard to the separation of the topography, no additional SAR images are needed if a DEM is available. The same holds if the baseline is short, say, some tens of meters, and the scene is rather flat, since then the topography can be neglected. Otherwise, at least three SAR images with sufficiently high coherence must be available to eliminate the topography.

Since one interferogram only shows the radar line-of-sight motion at least three observa-

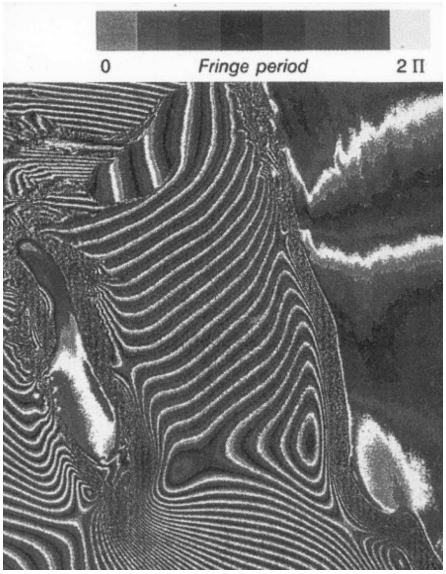

Figure 31: SAR interferogram of the Filchner-Ronne shelf ice in the Antarctic, from (Hartl et al. 1994). Temporal baseline is 3 days. The interferogram shows on the right side the western slope of Berkner Island resting on bedrock, and on the left Hemmen Ice Rise grounded on sea-bed shoals and surrounded by the floating Ronne Ice Shelf. The fringes on the Ronne Ice Shelf reflect the motion of the Filchner-Ronne shelf ice over three days, the topography, and the effect of ocean tides.

tions with different orientations are needed to determine the three-dimensional velocity field. Combining successive ascending and descending SAR images can provide two observations if the crossing angle between ascending and descending orbit is not too small. In case of the ERS satellites it is about 48 degrees over the Antarctic. Usually, the missing third observation is replaced by the surface slope derived from InSAR and the assumption that the ice flow is parallel to the surface topography, i.e. in the direction of the maximum slope. Then, it is possible to eliminate up to a certain extent the vertical flow component yielding the horizontal velocity in the across track direction.

InSAR has also been applied to monitor surface changes in ice covered regions. For instance, Figure 33, taken from (Thiel et al. 1997) shows two interferograms of the area around the Vatnajökull volcano in Iceland. The volcano erupted on September 30, 1996 after an earthquake with a magnitude of 5.4 on the Richter scale. The images have been acquired at October 21 and 22, 1996, during the ERS-1/2 tandem mission. The interferogram on the left shows the fringes due to the topography and the surface deformation. After removing the effect of the topography, the remaining fringes express the surface changes over 1 day due to the eruption of the Vatnajökull volcano (right interferogram in Figure 33). Various areas can be identified which show large deformations of up to 25 fringes corresponding to 80 centimeters deflation within one day. Some areas can be identified as well, which are completely decorrelated, partially because the deformations

Figure 32: Differential SAR interferogram of the Filchner-Ronne shelf ice in the Antarctic showing differences in the tidal signal at the data acquisition times, from (Hartl et al. 1994). The rise and fall of the ocean tide and the seaward movement of the ice can be seen in the fringe pattern towards the top of the image.

are that large that coherence is lost and no fringes show up.

Although InSAR has shown to be a promising technique for monitoring glaciers and ice sheets, we are still far from exploiting its full potential. Too many problems are still not yet fully solved. For instance, present satellites with a SAR as payload do not fully cover polar regions. ERS-2, for example, cover to 82 degrees leaving a gap of about 8 degrees at the poles. In addition, Greenland and polar regions suffer from severe weather conditions which may lead to complete decorrelation within a few days, e.g. due to snow storms, melting, blowing snow etc. Finally, atmospheric signals may corrupt the interferograms.

Acknowledgment: A. Smits from the Department of Geodesy at Delft University of Technology prepared the figures. His support is gratefully acknowledged.

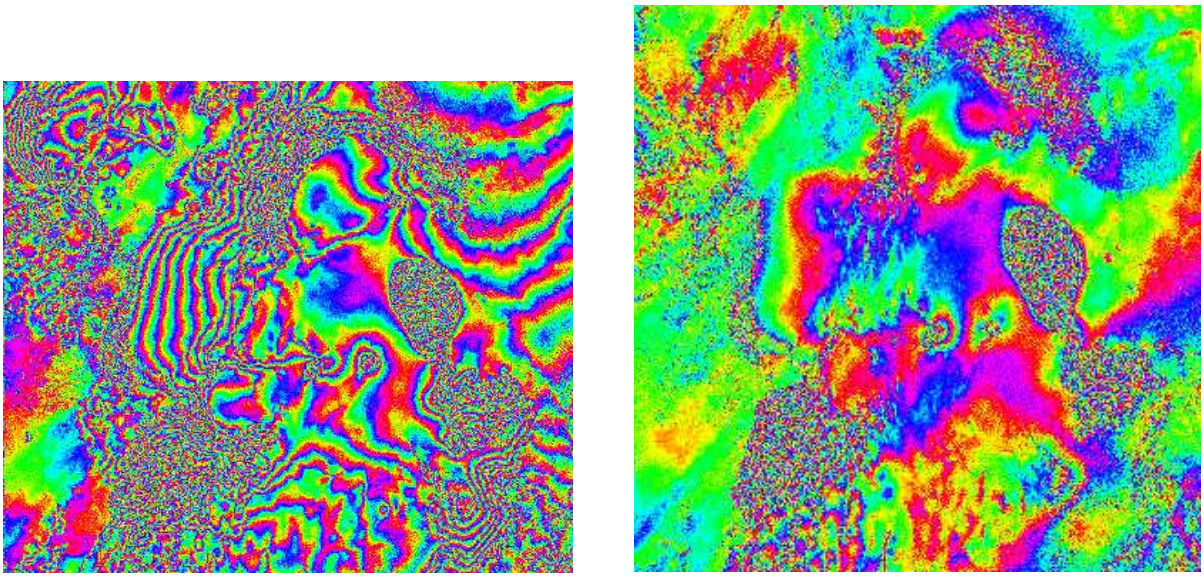

Figure 33: Interferograms of the area around Vatnajökull volcano on Iceland formed by SAR images acquired at October 21 and 22, 1996. Topography (left) and surface deformation (right). One fringe corresponds to about 72 m elevation change (left) and 3 cm vertical deformation (right), respectively. From (Thiel et al. 1997).

References

Amelung, F., S. Jonsson, H.A. Zebker, and P. Segall (1999), *Prospects of volcano geodesy with ERS radar interferometry*, Second International Workshop on ERS SAR Interferometry, 'FRINGE 99', Liege, Belgium, 10-12 Nov, p. 5, ESA.

Curlander J.C., and R.N. McDonough (1991), *Synthetic Aperture Radar, Systems and Signal Processing*, John Wiley & Sons, Inc., New York, 1991.

Dixon, T. (ed.) (1995), *SAR interferometry and surface-change detection*, University of Miami Technical Report TR 95-003, Miami, 97 p.

Ghiglia, D.C., and M.D. Pritt (1998), *Two-Dimensional Phase Unwrapping*, John Wiley & Sons, Inc., New York, 1998.

Hanssen, R.F. (2001), *Radar interferometry: data interpretation and error analysis*, Ph.D. thesis, Department of Geodesy, Delft University of Technology, The Netherlands, 2001.

Bamler, R., and P. Hartl (1998), *Synthetic aperture radar interferometry*, Inverse Problems 14: R1-R54.

Hanssen, R.F., T.M. Weckwerth, H.A. Zebker, and R. Klees (1999), *High-resolution water vapor mapping from interferometric radar measurements*, Science, 283: 1295-1297.

Hanssen, R.F. (1998), *Atmospheric heterogeneities in ERS tandem SAR interferometry*, DEOS Report no. 98.1, Delft University Press, The Netherlands.

Hartl, P., K.H. Thiel, X. Wu, C. Doake, and J. Sievers (1994), *Application of SAR interferometry with ERS-1 in the Antarctic*, Earth Observation Quarterly, 43: 1-4.

Klees, R. and D. Massonnet (1999), *Deformation measurements using SAR interferometry: potential and limitations*, Geologie en Mijnbouw, 77: 161-176 and 196-201.

Massonnet, D., and K. Feigl (1998), *Radar interferometry and its application to changes in the Earth's surface*, Rev. Geophys. 36: 441-500.

Massonnet, D., M. Rossi, C. Carmona, F. Adragna, G. Peltzer, K. Feigl, and T. Rabaute (1993), *The displacement field of the Landers earthquake mapped by radar interferometry*, Nature, 364: 138-142.

Massonnet, D., P. Briole, and A. Arnaud (1995), *Deflation of Mount Etna monitored by space-borne radar interferometry*, Nature, 375: 567-570.

Massonnet, D. and F. Sigmundsson (2000), *Remote sensing of volcano deformation by radar interferometry from various satellites*, In: P.J. Mouginis-Mark, J.A. Crisp, and J.H. Fink (Eds.), Remote Sensing of Active Volcanism, Geophysical Monograph 116, American Geophysical Union, Washington, DC: 207-221.

Thiel, K.-H., X. Wu, and P. Hartl (1997), *ERS-Tandem-interferometric observation of volcano activities in Iceland*, Proc. 3rd ERS Symposium 'Space at the service of our environment', Florence, Italy, 17-21 March 1997, ESA Publication, Noordwijk, SP 414, I: 475-480.

Usai, S., C.D. Gaudio, S. Borgstrom, and V. Achilli (1999), *Monitoring terrain deformations at Phlegrean Fields with SAR interferometry*, Second International Workshop on ERS SAR Interferometry, 'FRINGE99', Liège, Belgium, 10-12 Nov 1999, page 5. ESA.

Zebker, H.A., F. Amelung, and S. Jonsson (2000), *Remote sensing of volcano surface and internal processes using radar interferometry*, In: P.J. Mouginis-Mark, J.A. Crisp, and J.H. Fink (Eds.), Remote Sensing of Active Volcanism, Geophysical Monograph 116, American Geophysical Union, Washington, DC: 179-205.